Deactivation of Pd/C catalysts by irreversible loss of hydrogen spillover ability of the carbon support

Laurent Vanoye, Boris Guicheret, Camila Rivera-Cárcamo, Jérémy Audevard, Javier Navarro-Ruiz, Iker Del rosal, I.C. Gerber, Cristian Campos, Bruno Fernandes Machado, Jérôme Volkman, et al.

Deactivation of Pd/C Catalysts by Irreversible Loss of Hydrogen Spillover Ability of the Carbon Support

Laurent Vanoye,[a] Boris Guicheret,[a] Camila Rivera-Cárcamo,[b] Jérémy Audevard,[b] Javier Navarro-Ruiz,[c] Iker del Rosal,[c] Iann C. Gerber,[c] Cristian H. Campos,[d] Bruno Fernandes Machado,[e] Jérôme Volkman,[b] Régis Philippe,[a] Philippe Serp,[b,*] Alain Favre-Réguillon[a,f,*]

[a] *Université Lyon, Catalyse Polymérisation Procédés & Matériaux (CP2M), UMR 5128 CNRS – CPE Lyon, 43 boulevard du 11 novembre 1918, F-69100 Villeurbanne, France.*

[b] *Université de Toulouse, ENSIACET, LCC CNRS-UPR 8241, F-31030 Toulouse, France.*

[c] *Université de Toulouse, INSA−CNRS−UPS, LPCNO, Toulouse F-31077, France*

[d] *Departamento de Físico-Química, Facultad de Ciencias Químicas, Universidad de Concepción, Edmundo Larenas 129, Casilla 160-C, Concepción, Chile*

[e] *University of Porto, Laboratory of Separation and Reaction Engineering – Laboratory of Catalysis and Materials (LSRE-LCM), Rua Dr. Roberto Frias s/n, 4200-465 Porto, Portugal.*

[f] *Conservatoire National des Arts et Métiers, EPN7-CG, F-75003 Paris, France.*

Abstract: General interest in solvent-free catalytic processes is driven by the development of environmentally and economically acceptable procedures. Such processes require the use of highly active and stable catalysts. This study reports on the synthesis, characterization, and kinetic evaluation of two highly active Pd catalysts supported on different carbons support, *i.e.*, multi-walled carbon nanotubes (CNT) and few-layer graphene (FLG). These catalysts, with similar Pd loading (~2 wt%) and containing both Pd single atoms (Pd_{SA}) and nanoparticles (Pd_{NP}), were systematically tested for solvent-free total hydrogenation of squalene (SQE) to obtain high-purity squalane (SQA). Thanks to the unique cooperative catalysis between Pd_{SA} and Pd_{NP} involving H-spillover, the activities of both catalysts were high compared to catalysts described in the literature. Solvent-free total hydrogenation of SQE could be performed under mild conditions (120 °C, 20 bar H_2, 4h) using ultralow Pd loading (60 ppm). However, since this reduction reaction is highly exothermic (ΔH_R= - 765 kJ.mol^{-1}), heat management during the reactor operation with these highly active catalysts is crucial to avoid deactivation and thermal runaway. Under these conditions, Pd/FLG was highly active but deactivated, unlike Pd/CNT, which still has high activity, but does not deactivate. Characterizations (ICP, XPS, Raman, TPD-MS, HAADF-STEM) of the Pd/FLG catalyst before and after reaction, supported by calculations based on density functional theory, allowed us to propose a new mechanism of catalyst deactivation involving the chemical reduction of specific surface oxygen groups of the carbon support induced by H-spillover.

Keywords: palladium, H-spillover, deactivation, solvent-free hydrogenation, carbon nanotube support

1. Introduction

One of the most common hydrogenation reactions performed in the fine chemical industry is the hydrogenation of carbon-carbon double bonds [1]. This transformation is considered a robust, atom-economical reaction, usually carried out with Ni-, Pt- or Pd-based heterogeneous catalysts. Wide varieties of catalysts are available from commercial suppliers, but careful catalyst design is required to obtain total conversion under mild conditions and reduce the use of critical metals [2-4]. One way to address this issue is to increase the metal dispersion. The ultimate dispersion achievable for a supported catalyst is where the metal atoms are all isolated from each other as in supported metal single-atom catalysts (SAC),[5] and numerous reviews can be found on this topic [6]. However, even if the chemical reactivity and cooperativity [7] of SAC are the objects of intensive research, the main challenge remains the catalyst production, stability, and characterization [8-10].

Recently, we have prepared new Pd-supported catalysts on carbon nanotubes (CNT) bearing both Pd nanoparticles (Pd_{NP}) and Pd single atoms (Pd_{SA}) [11,12] and have demonstrated that these two Pd species cooperate thanks to H-spillover on the carbon support [12]. In these catalysts, molecular hydrogen is readily dissociated on Pd_{NP}, and the activated hydrogen reaches the hydrogenating site (the Pd_{SA}) via H-spillover. We have shown that controlling the ratio between Pd_{SA} and Pd_{NP} on carbon supports enables the design of very active hydrogenation catalysts integrating the ultra-rational use of precious metals [12-14]. These new catalysts may meet the need to increase catalytic activity for highly demanding substrates and conditions, like the solvent-free total hydrogenation of bio-based squalene (SQE) into squalane (SQA) (Scheme 1) [15-17].

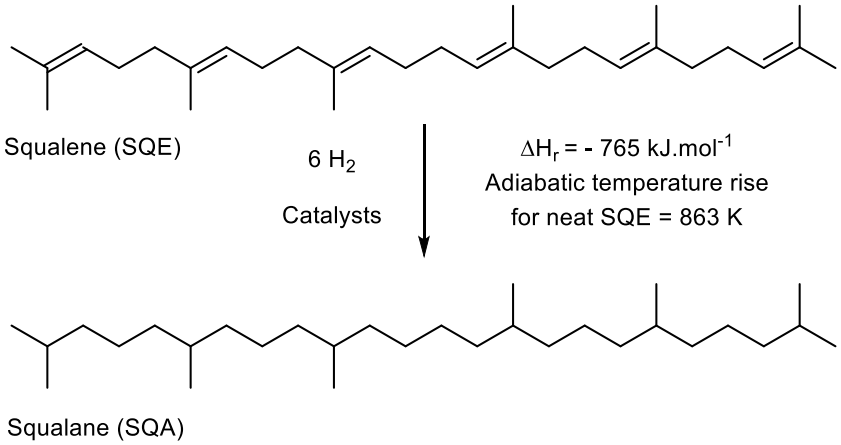

Scheme 1. Hydrogenation of squalene (SQE) into squalane (SQA)

The solvent-free total hydrogenation of SQE is linked to safety issues due to the exothermicity of the reduction (ΔH_R = -765 kJ.mol^{-1}). An adiabatic temperature rise higher than 860 K could be calculated for such conditions. Furthermore, the problem of the catalysts' stability arises from this highly exothermic hydrogenation reaction. We recently reported the excellent performances of Pd/CNT catalysts containing an optimized concentration of Pd_{SA} and Pd_{NP} for SQE hydrogenation [13,17]. With the objective of improving the catalyst's design, we propose an optimization of the communication channel between Pd_{NP} and Pd_{SA}, namely the H-spillover. To do this, we used a support favoring spillover, few-layer graphene (FLG). Herein, we compare the performance of the Pd/CNT and Pd/FLG catalysts, including activity and stability for the demanding solvent-free SQE total hydrogenation.

2. Materials and methods

Squalene and solvents. SQE (98%) and heptane were purchased from Aldrich and used as received. SQE was stored under refrigeration (2-8°C) and protected from light.

Catalyst supports. The CNT and FLG supports were produced and oxidized according to a procedure described elsewhere [11]. For CNTs, an $AlFeCoO_4$ catalyst was reduced in a fluidized bed reactor under a nitrogen (225 $mL \cdot min^{-1}$) and hydrogen (150 $mL \cdot min^{-1}$) flow at 650 °C. After the reduction step, an ethylene flow was adjusted to 225 $mL \cdot min^{-1}$ for 30 min to produce CNTs. The CNTs were recovered and then purified using an aqueous solution (50 vol% H_2SO_4) under reflux at 140 °C for 3 h. The acidic solution was then filtered, and the solid was washed with distilled water. The resulting solid was dried in an oven at 80 °C overnight. The purified CNTs were then functionalized with HNO_3 under reflux at 140 °C for 3 h. The acidic solution was filtered and washed with distilled water. The resulting solid was dried in an oven at 80 °C overnight to produce functionalized CNT. For FLG, a $CoFe_2O_4$ catalyst was reduced in a fluidized bed reactor under a nitrogen (225 $mL \cdot min^{-1}$) and hydrogen (150 $mL \cdot min^{-1}$) flow at 650 °C. After the reduction step, the ethylene flow was adjusted to 225 $mL \cdot min^{-1}$ for 30 min to produce FLG. The FLG was recovered and purified at room temperature overnight using HCl. The acidic solution was then filtered and washed. The resulting solid was dried in an oven at 80 °C overnight. The purified FLG was then functionalized with HNO_3 under reflux at 140 °C for 3 h. The acidic solution was filtered and washed. The resulting solid was dried in an oven at 80 °C overnight to produce functionalized FLG.

Palladium catalysts. Pd/CNT and Pd/FLG were prepared by wet impregnation method according to P. Serp *et al*. [12]. Briefly, a desired amount of $Pd(NO_3)_2.2H_2O$ (1.2 %w/w of Pd) was added to 100 mL of acetone with 1 g of the oxidized carbon support. The solution was sonicated at rt for 1 h and magnetically stirred overnight. After filtration and acetone washing,

the resulting solid was dried at 120 °C overnight and reduced in a horizontal tube oven under an 80% N_2/20% H_2 flow at 300 °C for 2 h.

Characterization of the catalysts. The palladium content was measured by inductively coupled plasma optical emission spectroscopy (ICP-OES). Elemental analyses of C and H were carried out on a PERKIN ELMER 2400 Serie II elemental analyzer. TEM and HR-TEM analyses were performed at the "Centre de microcaracterisation Raimond Castaing, UMS 3623, Toulouse" by using a JEOL JEM 2100F equipped with a field emission gun (FEG) operating at 200 kV with a point resolution of 2.3 Å and a JEOL JEM-ARM200F Cold FEG operating at 200 kV with a point resolution of > 1.9 Å. The particle size distribution was determined by manually measuring enlarged micrographs from different areas of the TEM grid (at least 300 particles). The size distribution reported as Pd atomic percentage (based on total atoms) in each size range was obtained by calculating the number of atoms (N) in each nanoparticle, assuming a spherical shape using an equation described in ref. [18]. The SA/NP ratio (a number ratio) was measured from the STEM-HAADF analyses of at least 3000 elements. The dispersion of Pd was calculated from a universal mathematical relationship between the average relative size of metallic crystallites and their dispersion [19].

The samples were analyzed by X-ray photoelectron spectroscopy (XPS) using a VG Escalab MKII spectrophotometer operating with a non-monochromatized Mg K source (1253.6 eV). XRD diagrams were measured at room temperature employing Cu-Kα radiation (λ = 1.54 Å) and a parabolic MPD mirror for Cu radiation. To measure the crystallite size L*c* (graphitic stacking), we used Sherrer's equation from the 002 line. Raman spectra were measured in a micro Raman Spectrometer HR 800 Jobin Yvon Horiba using a laser of 532 nm wavelength as an excitation source. The specific surface area and pore size distribution were determined from N_2 adsorption/desorption isotherms at – 196 °C using a Micromeritics instrument. Before analysis, all samples were degassed under vacuum at 120 °C for 6 h. The calculation of the

DFT, basal plane, and "non-basal plane" surfaces and the respective ratios has been performed as described in the literature [20,21].

Temperature programmed desorption (TPD) measurements were carried out using the 3Flex (Micromeritics) combined with a mass spectrometer (Cirrus 2, MKS Spectra Product). The sample (around 50 mg) was pre-treated under He (50 mL/min) at 120°C (10 °C/min) for 1 h to clean the surface. The sample was reduced at 150 °C for 2 h at 5 °C/min under 5% H_2/Ar flow. The solid was then purged with He at 50 °C until the TCD baseline remained stable prior to start with the temperature-programmed desorption at 10 °C/min ramp until 1000 °C. The products released were analyzed by mass spectroscopy. The following fragment (m/z) were recorded: 2, 15, 18, 28, and 44, corresponding to hydrogen (H_2), methane (CH_4), water (H_2O), carbon monoxide (CO), and carbon dioxide (CO_2), respectively.

Hydrogen spillover evaluation. To check for the H-spillover, we used WO_3 to diagnose the activation of H_2 in the various catalysts because the spilled-over hydrogen migrates and readily reacts with the yellow WO_3 to form dark blue H_xWO_3 [22]. Samples made with 1 g of WO_3 were mixed or not with 2.5 mg of catalyst (Pd/CNT or Pd/FLG) and treated with H_2 (40 mL/min) at 20 °C for 2 min. A test with Pd/FLG catalyst (2.5 mg) diluted in pure FLG (2.5 mg) was also performed.

General procedure for the hydrogenation of SQE in a stirred tank reactor. The reaction was performed in a 200 mL thermo-regulated stainless steel autoclave from Top Industrie. A stainless steel insert with four baffles was mounted on the reactor walls, and the reaction medium was stirred by a gas-inducing Rushton impeller having six straight blades. Temperature control is provided by an electric shell (for heating) and a Ranque-Hilsch vortex device (for cooling). The reactor is operated in batch mode for the liquid and solid phases and semi-batch mode for the gas phase. Hydrogen was constantly fed via a pressure regulator and supplied by a calibrated reserve. The pressure and temperature monitoring of this reserve provides the

hydrogen consumption rate. The time course of this consumption was acquired with a pressure transducer and recorded online using Labview® at 1 Hz.

The catalyst and 80 mL of neat SQE, with tetradecane (0.1 M) as an internal standard, were placed in the reactor. The reactor was purged three times with N_2 at room temperature, and the reactor was heated up to the desired temperature under stirring. When the desired temperature was reached, stirring was stopped. The N_2 atmosphere was replaced by the H_2, and the experiment was started by switching on the agitator, determining the t_0 of the reaction.

Unlike other terpenes, the reactivity of the double bonds in SQE is quasi-identical (all tri-substituted double bonds). As such, identifying different isomers as the function of time by classical GC/FID and GC/MS methods is impractical since up to 150 isomers and diastereoisomers could theoretically be formed [13,17]. However, in-line H_2 consumption associated with off-line GC analysis at the end of each experiment could give highly reproducible monitoring of the reaction mixture. Thus, the reaction progress, i.e., the number of moles of H_2 consumed per mol of SQE, could be plotted as a function of time. The derivatization of these plots allows us to obtain the hydrogen consumption rate as the function of the reaction progress for the different catalytic tests. The reaction mixture was analyzed at the end of each test. After dilution with heptane using an Agilent 6890 GC-FID equipped with DB-17 columns, the total conversion of SQE was confirmed.

Computational Details. Periodic Density Functional Theory (DFT) calculations were performed using the *ab initio* plane-wave pseudopotential approach implemented in the Vienna Ab initio Simulation Package (VASP; version 5.4) [23,24]. The exchange-correlation potential was approximated with the generalized gradient approximation to the Perdew–Burke–Ernzerhof [25] functional, and van der Waals interactions were taken into account through the D3 correction method of Grimme *et al*. [26]. The core electrons were modeled using the Projector Augmented Wave (PAW) approach,[27,28] and the valence monoelectronic states

were expanded using a plane wave basis set with a cutoff energy of 450 eV. Partial occupancies were estimated with a Gaussian smearing (σ) of 0.05 eV during all relaxations and extrapolating the energies to σ = 0.00 eV. As recently computationally modeled and described,[29] the palladium-supported catalyst consists of O-functionalized graphene (including experimentally probed abundant oxygen functional groups and point defects) as the carbon support, along with a single Pd atom in a single vacancy and an ultra-small Pd_{13} nanoparticle as supported metal catalysts, the latter being hydrogenated with a H/Pd atomic ratio above unity. Γ-Centered (3×3×1) *k*-point mesh generated using the Monkhorst–Pack method [30] was employed, and all the systems were considered neutral. A vacuum region by at least 15 Å between the periodically repeated slabs was added to eliminate spurious interactions, and a dipole correction along the *z*-direction has been considered [31]. All structures were optimized until forces were less than 0.015 eV $Å^{-1}$. Transition states were first located using the Climbing Image version of the Nudged Elastic Band, CI–NEB method,[32,33] and then properly optimized using the Quasi–Newton algorithm. Finally, they were proven to show a single imaginary frequency by the diagonalization of the numerical Hessian matrix with a step of 0.015 Å in both positive and negative directions of each coordinate.

3. Results and discussion

Our groups recently reported that Pd/C catalysts showed high activity for the hydrogenation of β-myrcene,[11,12] and SQE in solution,[13] and neat [17]. A structure-activity correlation was evidenced, integrating three catalyst structural features: metal dispersion, amounts of surface oxygen groups, and defective sites on the support [11]. While the presence of metal dispersion in such a correlation was not surprising, the role of surface defects and oxygenated surface groups was less straightforward. Then, it was demonstrated that Pd_{SA} stabilized by surface defects of the support [34] and Pd_{NP} were simultaneously present on the carbon supports [12]. Unique cooperative catalysis operates between these species, allowing one to reach very high activity for alkene hydrogenation through an H-spillover assisted mechanism involving the support of oxygenated surface groups [12]. On carbon supports, oxygen surface groups have been reported to facilitate the H-spillover on Pd catalysts [35,36]. The observed cooperativity involved: i) H_2 activation on Pd_{NP}, ii) H-spillover on the support that enables the formation of H-Pd_{SA} species, and iii) the catalytic reaction on H-Pd_{SA} species, which are much more active than H-Pd_{NP} species for alkene hydrogenation and isomerization [12]. A similar cooperative effect between metal single atoms and nanoparticles has been recently reported for various hydrogenation reactions [7,14,37-40]. In catalysis, understanding the structure-activity relationship allows the rational design of the catalyst. In the present case, this should involve: i) controlling the ratio Pd_{NP}/ Pd_{SA}; and ii) optimization of the H-spillover. The Pd_{SA}/Pd_{NP} ratio was indeed found to play a prominent role in the observed catalyst activity for mesoporous carbon supports. The optimum Pd_{SA}/Pd_{NP} ratio was found on CNT support at 10/1 for myrcene hydrogenation [12]. This optimum corresponds to a high enough concentration of Pd_{NP} to insure H-spillover through the oxygen surface groups of the carbon support to feed the Pd_{SA} in H species. This optimum also corresponds to a high enough concentration of very active H-Pd_{SA}

species. We demonstrate below how the support choice can influence the H-spillover and, consequently, the catalytic performance.

3.1 Characterization of carbon supports

Two carbon supports were used in this study: CNT and FLG. The two supports were oxidized with nitric acid to introduce surface oxygen groups on their surface [11]. Since the physicochemical properties of the support can influence both catalyst performance and stability [35], the textural and structural properties (Table S1 for chemical, textural, and crystallite properties) and surface chemistry of the two materials were investigated. Figure S1 shows representative SEM, TEM, and HRTEM micrographs of the two materials. The FLG powder is composed of agglomerates of size 80-100 μm and thickness of 2-20 nm [41]. The CNT powder is composed of agglomerates of size 10-100 μm, and the mean external diameter of CNT is 13 nm. Compared to CNT, the FLG support shows a lower specific surface area (50 $m^2\ g^{-1}$ compared to 220 $m^2\ g^{-1}$ for CNT) and pore volume. DFT calculations derived from N_2 adsorption data [20,21] were used to determine the basal plane, prismatic, and defect surfaces of these two materials. Figure S2 depicts the adsorptive potential distributions and the ratios of prismatic: basal: defect surfaces of FLG and CNT. The highest proportion of the basal surface area is observed for CNT, while FLG presents a higher proportion of prismatic surface (edge sites). The fact that the FLG presents a significant amount of layers (5-50) explains this result. The I_D/I_G ratio (from Raman analyses) is lower for FLG, indicating a lower concentration of structural defects on this support. The crystallite size (L_c from XRD) and the typical inter-defect distance (L_D from Raman [42]) are higher for FLG than CNT. Overall, the structural analyses indicate a higher graphitization degree of the FLG support, which present a higher proportion of edge sites than CNT.

The surface chemistry of both materials, which can influence H-spillover,[35,43] was probed by TPD and XPS analyses. In XPS, the presence of defects and functional groups in carbon materials introduce new peaks and alter the peak position and line width of the C 1s peak. The best fit for the main C 1s spectrum was obtained by deconvoluting the profile into seven line shapes [44] (Figure S3), and their respective parameters and attributions are given in Table S2. The C/O atomic ratio was 16.5 for CNT and 25.3 for FLG, indicating a higher oxygen concentration per gram of material on CNT. This result can be rationalized by a higher proportion of defects on the pristine CNT and by their higher surface area. The quantification of surface functional groups presented in Table S2 shows that CNT contains a higher amount of them. The full width at half-maximum (FWHM) of the C 1s peak has been used to assess the graphitic nature of carbons, with a larger FWHM corresponding to a more disordered structure [45]. The obtained values (0.72 eV for CNT and 0.69 eV for FLG) confirm the higher graphitization degree of FLG. TPD-MS analysis allows characterizing oxygen-containing surface groups of carbon materials,[46] which decompose, releasing CO and/or CO_2 at different temperatures. The CO_2 and CO spectra of both materials are shown in Figure S4, and the quantification of these groups is shown in Table S3. The CNT and FLG support contain carboxylic acids of various strengths (CO_2 at 200/300 °C),[47,48] carboxylic anhydrides (CO_2 and CO at ~450-480 °C),[47,49,50] lactones (CO_2 above 600 °C),[47,49,50] phenols (CO at ~600-700 °C),[47,50] ethers and ketones (CO at ~650-750 °C),[47,50-52] and quinones/pyrones/chromenes (CO at T > 900 °C) [47,49,51] surface groups. Based on a mass basis, the concentration of all of these groups is higher on CNT than on FLG because of the higher specific surface area of CNT. However, if we consider the concentration of these groups per square meter of support, it is significantly higher for FLG (Figure S4, and Table S3). For FLG, these groups should be concentrated on the edges of the material, while in the case of CNT, they are evenly distributed over the whole surface [53].

3.2 Preparation and characterization of the Pd/C catalysts

Two Pd catalysts with a nominal Pd loading of 2 wt % were prepared by wet impregnation from Pd nitrate. From ICP analyses, the Pd loading were 2.04 % wt% and 1.87 wt % for Pd/CNT and Pd/FLG, respectively. The mean Pd_{NP} size and the Pd_{SA}/Pd_{NP} ratio (a number ratio) were determined from STEM-HAADF analyses. The measured mean Pd_{NP} sizes were 1.5 nm and 2.1 nm for Pd/CNT and Pd/FLG, respectively (Figure S5). The smaller Pd_{NP} size obtained on CNT should be related to a higher amount of oxygen surface groups well distributed on the CNT surface that can act as nucleation centers for Pd_{NP},[54] and to the higher surface area of CNT. Noteworthy, on FLG, the Pd_{NP} are mainly located on graphene edges, which are decorated by oxygen functional groups and act as nucleation centers for Pd_{NP} [55] whereas Pd_{NP} are more homogeneously distributed on the CNT surface (Figure 1).

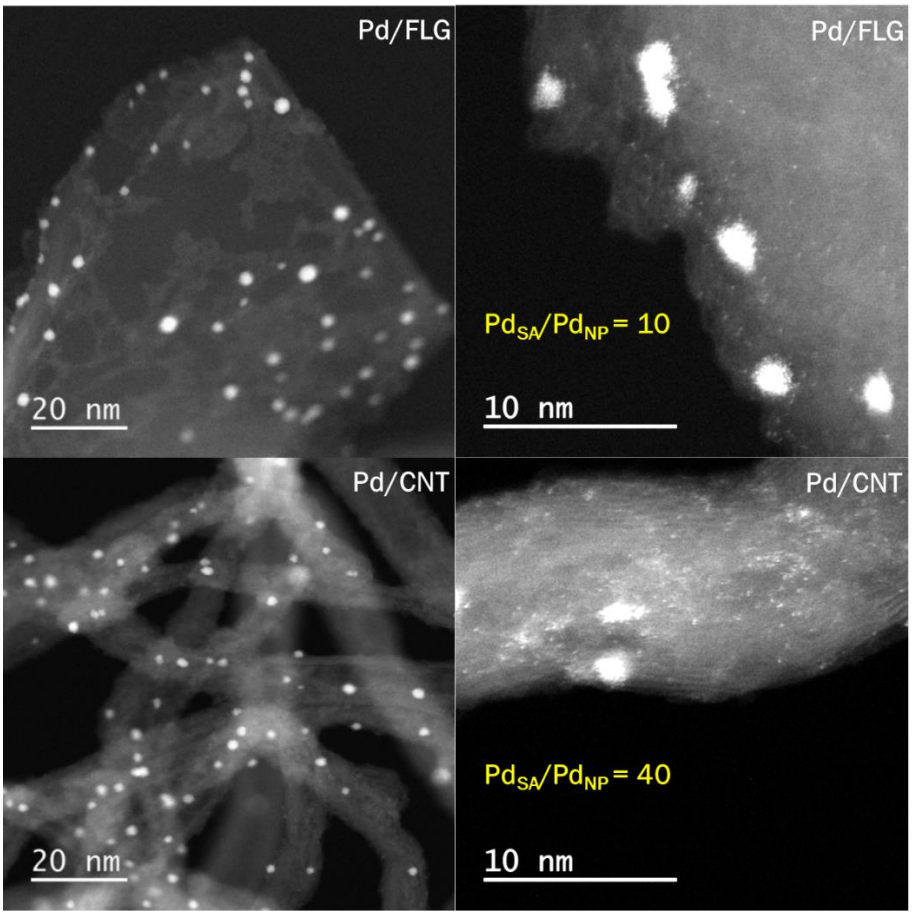

Figure 1. STEM-HAADF micrographs of the fresh Pd/FLG and Pd/CNT catalysts.

The Pd_{SA}/Pd_{NP} ratio was 40 for Pd/CNT and 10 for Pd/FLG (Table 1). The coexistence of Pd_{SA} and Pd_{NP} on both catalysts is visible in Figure 1 (additional micrographs are given in Figure S6).

Table 1. Catalysts' main characteristics

Catalyst	Pd content (wt%)	BET surface area ($m^2.g^{-1}$)	Particle size (nm)[a)]	Pd dispersion (%)	Pd_{SA}/Pd_{NP} ratio
Pd/CNT	2.04	232	1.5 ± 0.6	67[b)]	40
Pd/FLG	1.87	50	2.1 ± 0.8	51[b)]	10

a) from TEM; b) metal dispersion was evaluated from a universal mathematical relation between the mean relative size of metallic crystallites and their dispersion, as described elsewhere [56].

The two catalysts were also characterized by XRD, XPS, and TPD/MS analysis. In XRD (Figure S7), due to the relatively low metal loading and high metal dispersion, the diffraction peak associated with Pd(111) was of too low intensity to be exploited. XPS analyses were performed on the two catalysts to probe the Pd oxidation state and the charge transfer (Figure S8 and Table S4). The deconvoluted XPS spectra for Pd 3d exhibit three pairs of doublets, assigned to $Pd^{(0)}$, $Pd^{\delta+}$, and Pd^{2+} species. The binding energy of the metallic feature is ≈0.5 eV higher than that of Pd bulk (335.1 eV), which may arise from the small size of Pd_{NP} [57,58]. The $Pd^{(0)}$ species should be associated with the larger Pd_{NP} that did not experience significant charge transfer with the support. The $Pd^{\delta+}$ species should be related to the smaller Pd_{NP} (clusters) and Pd_{SA} that experienced significant charge transfer with the support. The Pd^{2+} species should correspond to surface oxidation (PdO). No significant differences were noticed as far as the $Pd^{\delta+}/Pd^{(0)}$ ratio is concerned (3.2 for both catalysts), and a slight difference in charge transfer (from the Pd to the support) was evidenced since the $Pd^{(0)}$ binding energy shifts from 335.50 eV for Pd/FLG to 335.65 eV for Pd/CNT (Figure S9). The higher Pd $3d_{5/2}$ value measured for the $Pd^{(0)}$ of Pd/CNT should be related to the smaller mean Pd_{NP} size measured for this sample. It should be noticed that the values of the $Pd^{\delta+}/Pd^{(0)}$ ratio did not reflect the values of the Pd_{SA}/Pd_{NP} ratio measured from STEM. This could be explained by the fact that in the Pd/FLG catalyst, more Pd_{NP} are experiencing charge transfer from the support since they are located on the prismatic surface of the support (edge surface) and not on the basal surface like in CNTs. Indeed, the largest charge transfer from Pd to carbon nanofibers presenting prismatic

surface was observed compared to Pd deposited carbon nanofibers presenting basal surface [59]. Additionally, the higher concentration of surface oxygen groups (per square meter of support) on the FLG support can contribute to a more intense charge transfer, as shown by Teyssonier *et al.* [58].

3.3 Hydrogen activation and hydrogen spillover

Density functional theory (DFT) calculations were performed to investigate H_2 activation on Pd_{NP} and Pd_{SA}. To do this, some of us recently developed a realistic model that integrates Pd_{NP} and Pd_{SA} on a carbon support decorated with oxygen functional groups is used [29]. In the case of Pd_{NP}, with no hydrogen atoms at the Pd surface (atomic ratio H/Pd = 0.00), dihydrogen is strongly coordinated on top of a Pd atom with an adsorption energy of -17.4 kcal·mol^{-1} (see Figure S10). The thermodynamics of the H_2 dissociation process is very favorable (-13.0 kcal·mol^{-1}), in addition to being easily accessible from the kinetics (energy barrier of 5.7 kcal·mol^{-1}). On the other hand, at high hydrogen coverage (atomic ratio H/Pd = 0.92),[29] the Pd_{NP} is close to H-saturation, and the coordination of H_2 is weaker (adsorption energy of -9.6 kcal·mol^{-1}, see Figure S10). The dissociation is still thermodynamically favorable (-6.3 kcal·mol^{-1}), although kinetically, it is more impeded (energy barrier of 10.0 kcal·mol^{-1}). For the Pd_{SA} case, H_2 can be easily adsorbed on the metal center (adsorption energy of -10.0 kcal·mol^{-1}). However, both homolytic and heterolytic H_2 dissociations are clearly endothermic (reaction energies greater than 10.5 kcal·mol^{-1} relative to the non-dissociated state, see Figure S11), so it will not take place. Thus, the only plausible way to form the Pd_{SA}−H species is through a H-spillover mechanism, dissociative H_2 adsorption on Pd_{NP} appears to be the first step in this process.

As far as H-spillover from Pd_{NP} to Pd_{SA} is concerned, thermodynamics indicates a slightly favorable overall process between Pd species of about -3.3 kcal·mol^{-1} (H atoms prone to spillover process). The corresponding reaction energies can be seen in Figure S12a). Therefore, the second step of the process corresponding to the migration of hydrogen from the Pd_{NP} to the

support is assessed. Previous studies have shown that spillover from a metal surface to a defect-free carbon support surface is difficult. It would not occur significantly under normal conditions, being rather endothermic and needing to overcome a large barrier, close to the desorption energy of hydrogen atoms on metal clusters [60]. However, spillover of H atoms from metal nanoparticles onto a defective carbon support or doped support is possible [35]. To probe the thermodynamics of the reaction on our aforementioned O-functionalized support, which was built from the data obtained by TPD-MS, the migration of hydrogen is studied using a –COOH motif as H-transfer group. Specifically, the surface concentration of carboxylic acid groups calculated experimentally was found to be 1.84 and 3.23 –COOH nm^{-2} for the CNT and FLG supports, respectively. Due to the flexible geometry of the acid group thanks to C–C rotation and C–O–H bending, the H atoms can jump, through a concerted mechanism, to several C atoms of the support. The H transfer takes place when one of the Pd_{NP} H atoms is transferred to the oxygen of the C=O fragment, while the H atom of the OH fragment migrates to the carbon support. The computed reaction energy depended on the relative position of the hydrogen with respect to the –COOH group, being the *ortho* and *para* positions the only energetically favorable (-12.6 and -8.3 $kcal \cdot mol^{-1}$ respectively, see Figure S12b). It should be noted that, to facilitate H spillover, the –COOH must be: i) close enough to both the Pd_{NP} and the C atoms arranged to saturate; and ii) non coordinated to Pd_{NP}, since they help the metallic species to remain deposited and, therefore, are not free to undergo hydrogen spillovers. In this case, the distance between the nearest H and the C=O fragment was 2.74 Å, while between the OH fragment and each of the two most favored C atoms was 2.19 and 2.93 Å, respectively.

Due to the oxygen functionalization of the carbon support, the Pd-supported catalyst model also presents carbonyl groups located next to point defects or decorating vacancies. Since some of them are located relatively close to Pd_{NP}, the H-spillover process through these carbonyl groups is also verified computationally (see Figure S13). The thermodynamics for the hopping of an H

atom from Pd_{NP} to a nearby C=O group is highly favorable compared to the previously studied –COOH group (reaction energy of -40.8 *vs.* -12.6 kcal·mol^{-1}, respectively), with C–OH being the only stable species (and not CH–O). In addition to the formation of the O–H bond, an intramolecular hydrogen bond with a neighboring C=O group appears, which could explain the high stability of this species. The distance between the H and O carbonyl atoms is 2.70 Å, very similar to the 2.74 Å distance between the H and O carboxylic atoms. Through a second H atom by spillover, the reduction of the carbonyl double bond is completed, giving rise to the formation of hydroxylated CH–OH species (the total reaction energy of the two steps turned out to be -41.4 kcal·mol^{-1}). This means that the C=O groups located in the vicinity of Pd_{NP} could be partially or totally saturated, leaving the hydrogen atoms almost trapped and not being able to undergo any spillover process. Therefore, the calculations suggest that the spillover process starts: i) after hydrogenation of all C=O groups in the vicinity of Pd_{NP}; or ii) by migration of the H atoms away from the Pd_{NP} thanks to the carboxylic groups.

Since the occurrence of H-spillover depends on the surface state of the carbon support (presence or lack of surface oxygen groups),[35] we also analyzed the catalysts by TPD/MS analyses (Figure S14 and Table S5). As expected, considering their decomposition temperature, the concentration of carboxylic groups decreases upon catalyst reduction at 300 °C, and a Pd(OOC-) interface is created for the two catalysts, associated with a narrow and intense peak characteristic of a catalytic decomposition located at 190 °C for Pd/CNT and 290 °C for Pd/FLG (Figure 2). Such surface acetato ligands have already been described in the case of Ru/CNT catalysts [61]. It is important to notice that the TPD has been performed on the reduced catalyst that has shown the air before the TPD experiments, so it is possible that the observed groups, including the acetato and carboxylic ones, have been created upon air exposure of the sample [61]. Furthermore, the persistence of carboxylic groups on the reduced Pd/CNT and Pd/FLG catalysts has been independently checked by XPS (Figure S15). Finally, the

temperature observed for the decomposition of these groups (190-290 °C) cannot be related to the desorption of adsorbed CO_2 from the support [62,63] or from Pd [64]. A different temperature of decomposition of the Pd-acetato interface on CNTs (190°C) and FLG (290 °C) is measured. Upon Pd deposition/reduction it is mainly the carboxylic groups decomposing at T < 300 °C that disappear and the new interface appear at 290 °C for FLG and 190 °C for CNTs (Figure S16). As the main difference between the two supports should be the location of these groups (on the edges for FLG and on the basal surface for CNTs), we can propose that the carboxylic groups on the edges should lead to a stronger interaction with Pd than the ones located on the basal surface. Several studies have already shown that the edge planes of some carbon materials (for example in carbon nanofibers) can interact much more strongly with metal atoms than the basal planes of CNTs do [65,66].

The amounts of CO_2 and CO released from the two supports differ (Table S5). Normalized by a gram of material, it is higher for Pd/CNT, but normalized by square meters of catalysts, it is significantly higher for Pd/FLG (Figure 2b). Considering that a higher concentration of surface oxygen functionalities should favor the H-spillover, the Pd/FLG sample should provide more H-spillover than Pd/CNT.

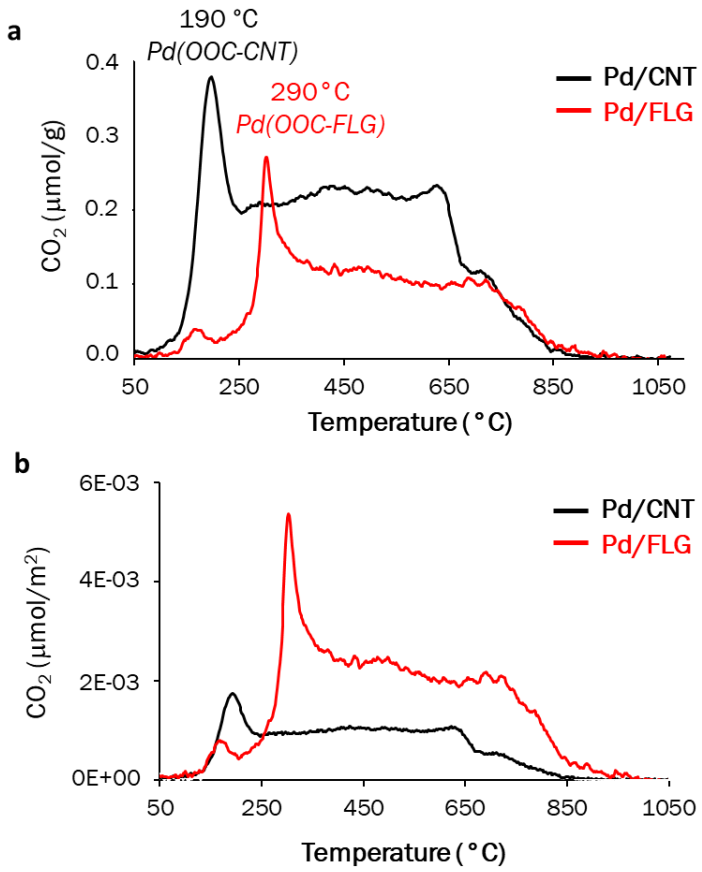

Figure 2. CO_2 TPD-MS spectra of Pd/CNT and Pd/FLG: a) CO_2 amount normalized by gram of catalysts; and b) CO_2 amount normalized by square meters of catalysts.

The H-spillover was experimentally probed for the two supported Pd catalysts. It is known that the spilled-over H species readily react under mild conditions with tungsten oxide WO_3 (yellow powder) to form dark blue H_xWO_3 [67]. Hydrogen molecules accomplish the reduction only above 200 °C [22]. As shown in the photographs of Figure 3, the WO_3 alone exhibited an unchanged color after H_2 treatment for 5 min at 20 °C. When mixed with 2.5 mg of the Pd/CNT catalyst, a slight change in color after the H_2 treatment was observed. Although this catalyst should activate dihydrogen, limited amounts of surface oxygen groups per square meter of support preclude extended H-spillover and WO_3 reduction. When the same amount of Pd/FLG (2.5 mg) is used, a darker color is observed according to a more extended reduction.

Dilution of the H-spillover active phase in a specific diluent, which is assumed to be the acceptor for spilled-over hydrogen species, has often been reported as an efficient strategy to improve catalytic performances in some hydrogenation reactions by limiting reverse H-spillover and recombination to molecular hydrogen [68,69]. Consequently, to confirm that hydrogen dissociation and H-spillover occurred on this catalyst, we also performed a test by diluting the Pd/FLG catalyst in pure FLG (2.5 mg of Pd/FLG + 2.5 mg of pure FLG), which should contain H spilled over acceptor sites. It is worth noting that, even in that case, we do not work at iso-surface (Pd/CNT = 232 $m^2 g^{-1}$; Pd/FLG = 51 $m^2 g^{-1}$; FLG = 50 $m^2 g^{-1}$). The evolution of the powder's color change (from darker to lighter) during this series of tests allows us to propose the following order for the H-spillover: Pd/FLG > Pd/CNT. We infer that the H-spillover should be attributed to the presence of specific surface groups (and their concentration) on the carbon support [35]. This series of experiments provided robust evidence that H-spillover does occur on these catalysts and is not consistent with an H transfer to WO_3 directly from Pd_{NP}. The higher surface group concentration on FLG (per surface unit) allows a more extended H-spillover.

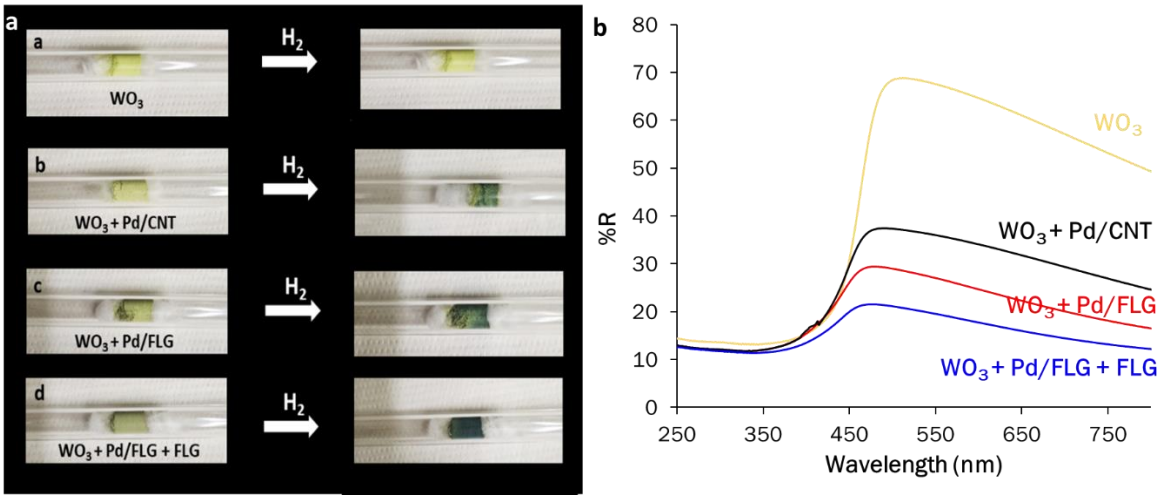

Figure 3. a) Photographs of samples made with 1 g of WO_3 mixed or not with catalyst before (left) and after (right) treatment with H_2 (40 mL/min) at 20 °C for 2 min: a) WO_3 alone; b) WO_3

+ 2.5 mg Pd/CNT; c) WO_3 + 2.5 mg Pd/FLG; and d) WO_3 + 2.5 mg Pd/FLG + 2.5 mg FLG. b) UV-Vis diffuse reflectance spectroscopy spectra of the resulting powders.

Besides activation of H_2 and H-spillover, we also consider the adsorption of a C=C bond of the alkene substrate on the Pd_{SA}. Because SQE is a large molecule with independent double bonds, it is interesting to apply a surrogate molecule mimicking unsaturated moieties as the essential motif to represent the C=C hydrogenation. In this case, the surrogate included a C5 organic molecule with a single double bond and is used as a probe reactant directly comparable to that of SQE. To account for both situations, the adsorption energies on a single Pd atom site before and after experiencing H-spillover (Pd_{SA} and Pd_{SA}–H) are computed (see Fig. S17). According to the calculations, the organic fragment was strongly accommodated on the Pd_{SA} species through an η^2-(C=C) coordination with values of -29 and -26 kcal·mol^{-1}, respectively. In terms of C=C activation, the distance of the double bond is 1.35 Å in the gas phase compared to 1.37 and 1.38 Å in the Pd_{SA} and Pd_{SA}–H species, respectively, so it is slightly activated. Thus, the SA sites are expected to be reasonably active for the hydrogenation of alkenes.

These characterizations reveal that both catalysts present similar particle sizes and few differences in charge transfer. However, if we integrate the cooperative catalysis that can operate thanks to H-spillover between Pd_{SA} and Pd_{NP} for alkene hydrogenation, an optimal Pd_{SA}/Pd_{NP} ratio, and an extended H-spillover were measured for the Pd/FLG catalyst.

3.4 Reduction of SQE with Pd/CNT and Pd/FLG

Since it has been previously shown that the activities of such catalysts are very high,[12,13,17] the amount of Pd was drastically decreased to 0.03 mol %. The solvent-free reduction of SQE was first studied with Pd/CNT under classical conditions, i.e., 120 °C, 20 bar H_2 (Figure 4a) [17]. Under those relatively mild conditions, the total and selective reduction of SQE into SQA was achieved in less than 80 min. This result demonstrates that the Pd/CNT catalyst combining

Pd_{SA} and Pd_{NP} can reach a very high activity for this reaction and is much more efficient under solvent-free conditions than those already described in the literature [15-17].

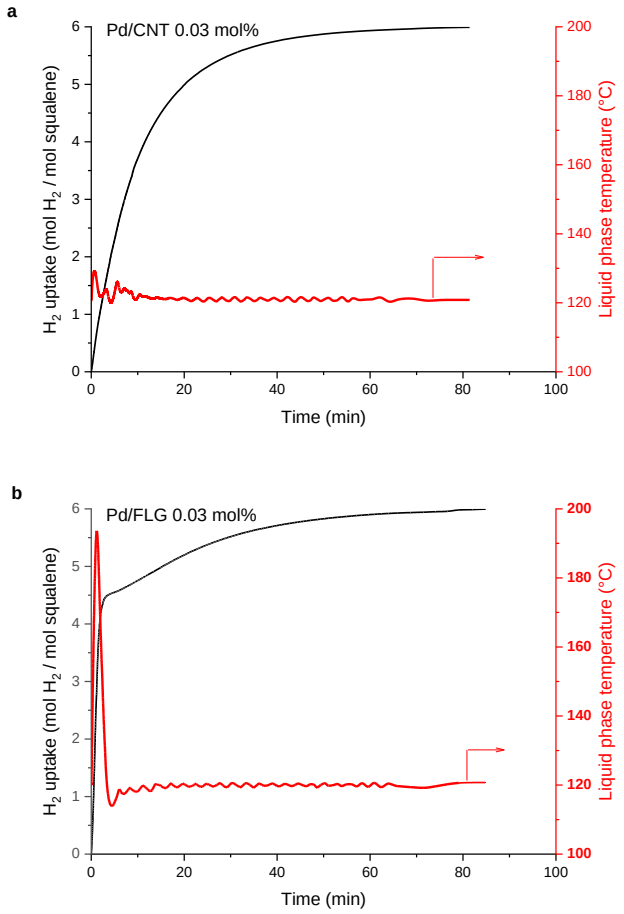

Figure 4. H_2 consumption and temperature as the function of time and catalysts. Reaction conditions: H_2 20 bar; 120 °C; liquid phase 80 mL of solvent-free SQE (2.03 M) with tetradecane as internal standard (0.1 M); a) Pd 0.03 mol % (270 mg of 2.04w% Pd/CNT); and b) Pd 0.03 mol % (290 mg of 1.87w% Pd/FLG).

Next, Pd/FLG was evaluated under the same condition (Figure 4b). Despite using an efficient Ranque-Hilsch vortex device for cooling the relatively small stirred tank reactor (200 mL), the liquid phase temperature reaches 190 °C within 1 min of reaction (Figure 4b). 75 % of the insaturations present in the liquid phase have been reduced within this first min, which results in a heat release of about 1460 W for 80 mL of liquid (up to 18 MW/m^3 of liquid), clearly raising safety issues when using this highly active catalyst for solvent-free reductions in a batch

reactor. The cooling device was able to decrease the liquid phase temperature back to 120 °C in about 3 min, and then the reaction can be completed at the reference temperature (i.e., 120 °C, Figure 4b). for the Pd/FLG catalyst, such an abrupt increase in liquid phase temperature has a conjugated effect on the intrinsic kinetics and on the H_2 solubility. This is undoubtedly the signature of higher initial intrinsic activity for this Pd/FLG compared to the Pd/CNT. Since both catalysts present similar particle sizes, the substantial improvement of the apparent catalytic activity observed for Pd/FLG could be explained by an optimal Pd_{SA}/Pd_{NP} ratio and H-spillover compared to Pd/CNT. Moreover, because of the temperature increase in these first 3 min, the catalytic activity of the Pd/FLG became affected by a G-L mass transfer limitation. Such a limitation masks the intrinsic catalytic activity of Pd/FLG and thus lowers the difference between the two catalysts.-Finally, the time to reach the total saturation of SQE with Pd/FLG was similar to Pd/CNT (Figure 4), and the deactivation of the Pd/FLG catalyst should be considered.

The Pd/substrate ratio was further decreased down to 0.006 mol % (60 ppm), and the catalysts were evaluated under the same conditions (Figure 5 a) and b). It should be noticed that, for such ultra-low Pd content, the maximum achievable concentration of Pd in the final product (SQA) if all the Pd introduced in the reactor will be leached out, which is highly improbable,[17] would be lower than 15 ppm (15 μg/g).

For both catalysts, and as expected, a slight temperature increase in the liquid phase could be noticed (Figure 5 a) and b). Surprisingly, even if the observed catalytic activity at low reaction progress was higher for Pd/FLG catalyst compared to the Pd/CNT catalyst (reaction progress of 2 was obtained in 32 min and 21 min for Pd/CNT and Pd/FLG respectively, (Figure 5 a) and b), the time needed to achieve the total hydrogenation of SQE was raised to 300 min for Pd/CNT and to more than 400 min for Pd/FLG. This could be explained by the deactivation of the

Pd/FLG catalyst. To probe the deactivation, the reaction rates of the different catalysts as the function of the reaction progress were compared (Figure 5 c) and d).

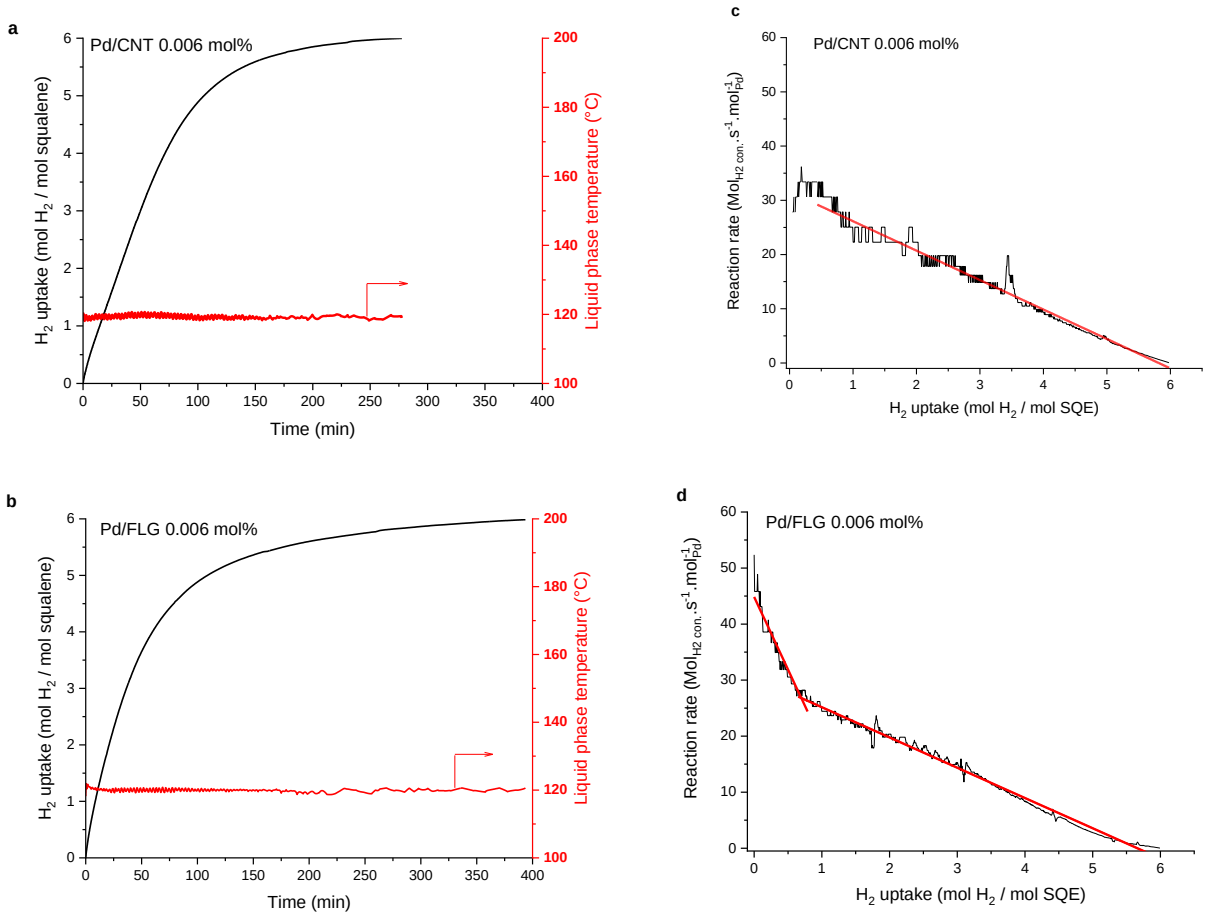

Figure 5. Comparison of the reaction progress as the function of the time and reaction rate as the function of the reaction progress for Pd/CNT and Pd/FLG during the solvent-free reduction of SQE. Reaction conditions: H_2 20 bar; 120 °C; liquid phase 80 mL of solvent-free SQE (2.03 M) with tetradecane as internal standard (0.1 M); a and c) Pd 0.006 mol%, 60 ppm (50 mg of 2.04w% Pd/CNT); b and d) Pd 0.006 mol%, 60 ppm (55 mg of 1.87w% Pd/FLG).

A fast non-linear decrease of the reaction rate against the reaction progress at the early stage of the reaction was noticed for Pd/FLG (Figure 5d), although this was not observed for Pd/CNT (Figure 5c). With such a low amount of Pd (0.006 mol %), no noticeable exothermicity could be detected in the liquid phase (Figure 5b), but internal exothermicity could explain the deactivation at the catalyst grain level. From Figure 2, it can be anticipated that Pd thermal stability issues could occur at T > 200 °C for Pd/CNT and at T > 300 °C for Pd/FLG.

To further probe the deactivation of the Pd/FLG catalyst, intentionally degraded operation conditions, which are generally implemented at the industrial scale,[70-75] i.e., two stages procedure, were used using 0.03 mol % of Pd (Figure 6). The first step was performed at 120 °C and low H_2 pressure (2 bar) to reduce the reaction rate strongly. When more than 60% of the theoretical hydrogen has been consumed (reaction progress ~ 4), an increase of the H_2 pressure from 2 to 20 bar was implemented to reach the complete transformation of SQE into SQA (Figure 6).

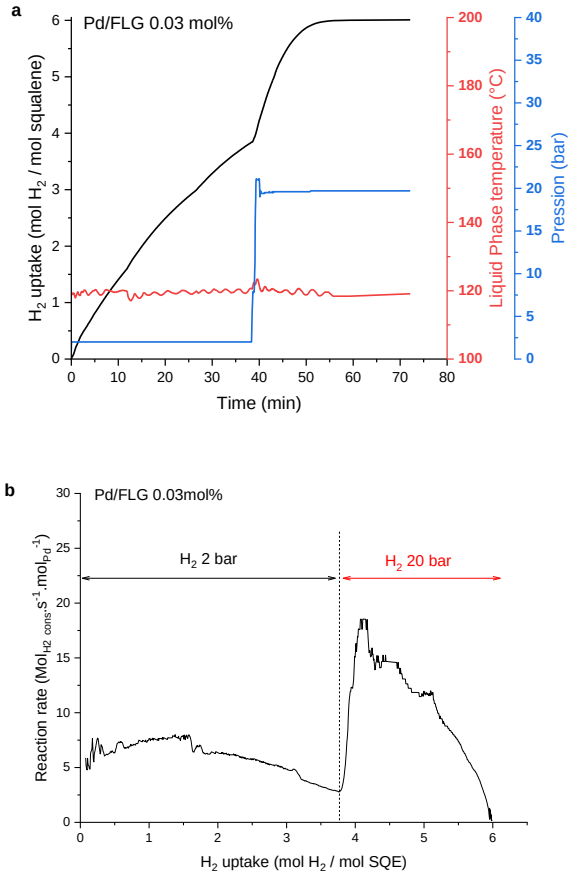

Figure 6. a) H_2 consumption and temperature as the function of time and H_2 pressure. b) Reaction rate as the function of the reaction progress. Reaction conditions: 80 mL of neat SQE (2.03 M), 120 °C, 290 mg of 1.87w% Pd/FLG (0.03 mol% Pd), H_2 2 bar for 40 min, then H_2 was increased to 20 bar.

As expected, a lower H_2 pressure induced a lower apparent reaction rate. Indeed it implies a lower solubility of H_2, thus both a lower reaction rate and a lower mass transfer rate (Figure 6a). In these deliberately downgraded conditions, an almost constant reaction rate of the catalysts as the function of the reaction progress could be observed (Figure 6b), and no exothermicity was noticed, as opposed to Figure 4b. Then, the H_2 pressure was raised to 20 bar (Figure 6a), and the reaction rate increased sharply (Figure 6b). Under those conditions, although not optimized, this two-stage procedure allows the total reduction of SQE in less than 60 min using 0.03 mol% of Pd. It should be noticed that the same amount of catalyst at constant H_2 pressure and pressure, i.e., 20 bar, 120 °C, up to 80 min, were necessary to obtain such yield but with safety issues (Figure 4b).

From these results, one can conclude that thanks to an optimal Pd_{SA}/Pd_{NP} ratio and extended H-spillover, the Pd/FLG catalyst is highly active. However, local thermal deactivation at the catalyst's surface occurs even at very low catalyst loadings without noticeable exothermicity in the liquid phase (Figure 5b and 6a). Even if Pd/CNT was slightly less active than Pd/FLG, no deactivation could be noticed with this catalyst.

3.5 Post-mortem characterization of the Pd/C catalysts

Sintering, coking, poisoning, or leaching are the major causes of palladium catalyst deactivation and premature degradation [76,77]. Since Pd sintering could be favored by the high exothermicity of the hydrogenation process, STEM-HAADF analyses were performed on the used catalysts to measure the mean Pd_{NP} size and Pd_{SA}/Pd_{NP} ratio after the reaction (Figure S18). The coexistence of Pd_{SA} and Pd_{NP} on both used catalysts is visible on the STEM-HAADF micrographs (Figure 7). The mean Pd_{NP} size was 2.1 nm and 2.0 nm for used Pd/FLG and Pd/CNT, respectively, whereas the mean Pd_{NP} size was 2.1 nm and 1.5 nm for fresh Pd/FLG and Pd/CNT, respectively. The Pd_{SA}/Pd_{NP} ratio was 9 and 25 for used Pd/FLG and Pd/CNT,

respectively, whereas the Pd_{SA}/Pd_{NP} ratio was 10 and 40 for fresh Pd/FLG and Pd/CNT, respectively.

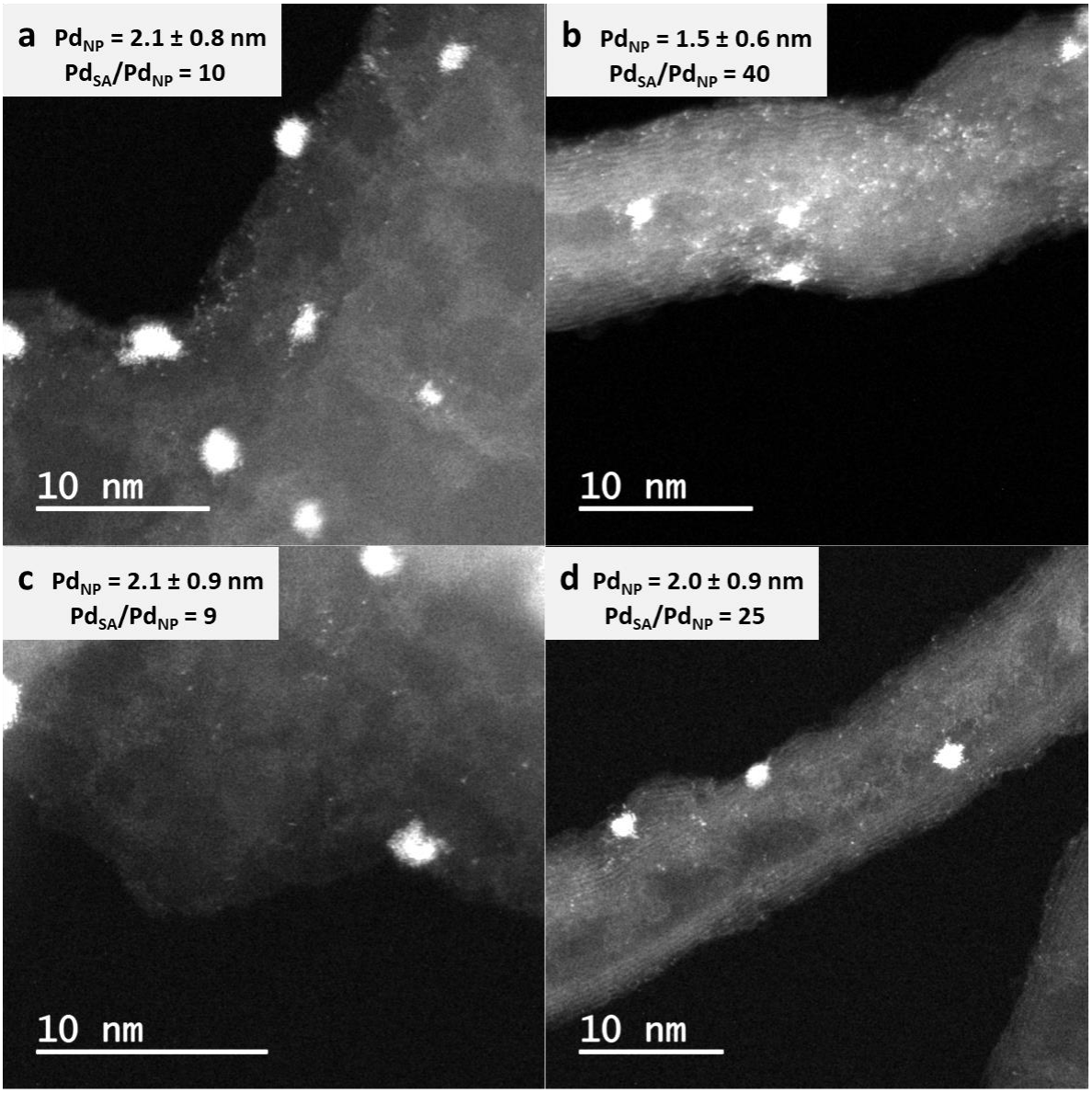

Figure 7. STEM-HAADF micrographs of **a)** the fresh Pd/FLG catalyst; **b)** the fresh Pd/CNT catalysts; **c)** the used Pd/FLG catalyst; and **d)** the used Pd/CNT catalysts. (scale bar = 10 nm).

On first analysis, these results may seem surprising because the Pd/FLG catalyst shows no sign of sintering, whereas the catalyst deactivates. The Pd/CNT catalyst shows a slight sintering and a decrease in the Pd_{SA}/Pd_{NP} ratio, which does not contribute to its deactivation. Further analyses were performed to find the origin of Pd/FLG catalyst deactivation. First, Pd assay by ICP-OES

for fresh Pd/FLG and used Pd/FLG catalysts, 1.70 %, and 1.69 % Pd w/w, respectively, does not reveal palladium leaching, which could be the cause of catalyst deactivation. Second, the high-resolution STEM and STEM-HAADF analyses of the used Pd/FLG catalyst (Figure S19) do not show the presence of a carbon deposit on the Pd_{NP} surface that could contribute to deactivation. It is worth mentioning that the used catalyst was filtered and washed thoroughly with heptane, so there is little chance of finding adsorbed SQE (SQA yield > 97%) or SQA, which, unlike SQE, is a very low-viscous molecule.

Considering the fact that the catalysis operates *via* cooperativity between Pd_{NP} and Pd_{SA} and that neither the size of the Pd_{NP} nor the Pd_{SA}/Pd_{NP} ratio has changed after the reaction, we can tentatively interpret the deactivation of the Pd/FLG catalyst as being related to a loss of communication between Pd_{NP} and Pd_{SA} due to a halt or a net slowing down of the H-spillover. This decrease in the H-spillover should be linked to a modification of the surface oxygen-containing functional groups of the Pd/FLG catalyst during the hydrogenation reaction. This phenomenon can be assisted by the H-spillover itself and by the exothermicity generated during the reaction. Indeed, it has been demonstrated that the H-spillover arising from noble metal nanoparticles facilitates the reduction of surface oxygen species on porous carbon materials,[64,78] or graphene oxide [43,79,80] at relatively low temperatures. Compared with H_2 reduction (H_2-molecule-involving reduction), H-spillover reduction (H-atom-involving reduction with extremely high reduction activity) can reduce the contents of oxygen surface groups of porous carbon more effectively [64]. The fact that this phenomenon does not occur for the Pd/CNT catalyst must be linked to the slightest local rise in temperature generated with this catalyst. Moreover, it is also interesting to note that it was reported that the high relative content of surface oxygen species and their distribution at the edges of FLG might lead to a cumulative effect that promotes the initiation of their decomposition [53]. This is not observed for CNT, showing surface oxygen species evenly distributed over the whole surface.

The decrease of surface oxygen species on the used catalyst was first evidenced by XPS analyses, which show an atomic percentage of surface oxygen of 8.6% in the fresh catalyst and 6.8% in the used catalyst. We rely on the O1s spectra to examine the surface species because all of the contributions belong to oxygen-functional species, and the overall intensity is higher as compared to the accompanying C1s signal due to the different atomic sensitivity factors. The assignments of specific features in the O 1s peak have been discussed in the literature [46,49,81-83]. It is generally agreed to the discrimination of four different oxygen species: peak I (530.5 eV) for C=O of quinones,[46,49,81] peak II (531.8-532.8 eV) for C=O of ketones, aldehydes or carboxyl,[46,49,81-84] peak III (532.6-533.8 eV) for -OH in phenolic species,[46,81,82] and peak IV (534.2 eV) for -OH group in carboxylic acids [49,81,84]. Both the fresh and used catalysts present these different species but in different proportions (Figure S20 and Table S6). Notably, the proportions of quinone (peak I), phenol (peak III), and carboxylic acid (peak IV) decrease in the used catalyst, whereas the proportion of carbonyl function (peak III) increases. We have also characterized by XPS the used Pd/FLG catalyst to measure the $Pd^{\delta+}/Pd^{(0)}$ ratio and compare it to the fresh catalyst. There is a significant change in the $Pd^{\delta+}/Pd^{(0)}$ ratio compared to the fresh catalyst. The $Pd^{\delta+}/Pd^{(0)}$ ratio is 3.2 (65 at. % of $Pd^{\delta+}$) for the fresh catalyst and 0.55 (34 at. % of $Pd^{\delta+}$) for the used catalyst. Since the mean Pd_{NP} size has not significantly changed between the fresh and used catalyst, we have attributed this difference to the fact that in the used catalyst the O/C ratio has significantly decreased, which impacts the work function of the support and, consequently the charge transfer from Pd NPs/clusters to the support. Such a phenomenon is known in the literature and has been reported by Teyssonier *et al*. [58].

CO_2-TPD was used to follow the concentration of the less stable oxygen surface groups on the fresh and used Pd/FLG catalyst (Figure 8a). Before the experiments, both samples were *in situ* treated under a 5% H_2/95% N_2 flow at 150 °C for 2 hours. After this treatment, most of the Pd(OOC-) interface has disappeared from the fresh catalyst, but this is not affecting the Pd_{NP} size. Most carboxylic acids (peaks at 175 and 300 °C) and part of the carboxylic acid anhydrides (peak at 520 °C) have disappeared on the used catalyst. Lactones (peak at 715 °C) have not been affected. Considering the fact that the presence of carboxylic acids is necessary for the H-spillover to operate, this decrease in carboxylic acids concentration should contribute to a net slowing down of the H-spillover. The fate of CO releasing groups was also examined (Figure 8b). The concentration of phenols and ketones significantly decreases for the used catalysts, whereas the more stable carbonyl functions have not been affected. These TPD analyses are consistent with the XPS analyses showing that the proportion of carbonyl groups is globally increasing. It is also noticed that new oxygen surface groups releasing CO at low temperature (250-450 °C) are also formed on the used catalyst (blue rectangle in Figure 8b). To get further insight into the catalyst deactivation mechanism, H_2-TPD analyses were performed (Figure 8c).

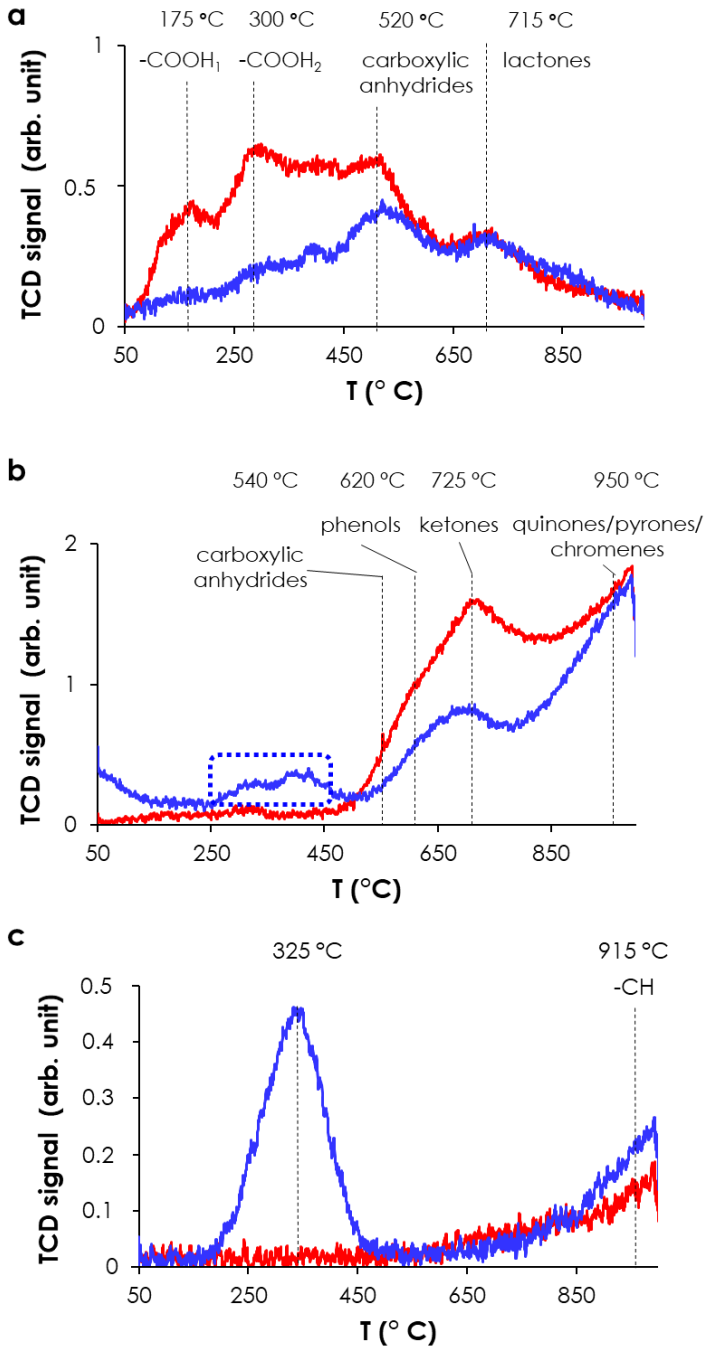

Figure 8. a) CO_2 TPD-MS spectra of fresh and used Pd/FLG catalysts; b) CO TPD-MS spectra of fresh and used Pd/FLG catalysts; and c) H_2 TPD-MS spectra of fresh and used Pd/FLG catalysts.

In the case of supported Pd catalysts, H_2 desorption from Pd species (either absorbed or chemisorbed H_2) has been reported to occur at relatively low temperatures, typically below

50°C [85,86]. Consequently, these desorption peaks are not visible in Figure 8c, which shows the desorption peaks associated with H_2 arising from the support. For the fresh catalyst, H_2 desorption starts at a relatively high temperature (> 650 °C). This high-temperature peak corresponds to stable C–H functionalities, which have been created by H-spillover from the Pd_{NP} [87]. This peak is more intense in the case of the used catalyst because it has experienced intensive H-spillover during the first minutes of the catalytic reaction. The most significant difference in the TPD profiles of the fresh and used catalysts is the presence of an intense and large peak centered at 325 °C for the used catalyst. This peak should correspond to the decomposition of new surface groups formed during the catalytic reaction thanks to H-spillover at a high local temperature. Considering the fact that the appearance of this peak corresponds to the appearance of new peaks in CO-TPD in the same temperature range, we can propose that the corresponding surface species should decompose by liberating both CO and H_2. Under the reducing conditions of the reaction, one can postulate that these newly formed functional groups could be primary and secondary alcohols, which is consistent with the release of H_2 and CO at around 350 °C during the TPD experiments. The thermal decomposition of isopropanol to H_2 and acetone has indeed been reported to occur at around 450 °C [88].

The formation of these new groups results from the reaction of oxygen surface groups with H-species resulting from spillover. The nature of the H-species, in the form of H^+, $H\cdot$, or both H^+ and $H\cdot$, depending on the nature of the support, has been discussed for a long time in the literature [89]. As far as carbon supports are concerned, the experimental and theoretical results obtained converge towards the fact that the majority of physisorbed $H\cdot$ are expected to associatively desorb as H_2 [35]. Spilled-over hydrogen can thus be seen as an unstable electron donor located at the surface, which needs to be stabilized. It could be stabilized by oxygenated species via the formation of carbonyl H-carriers, as proposed for H-spillover on non-reducible oxides,[90] where surface oxygen-containing functional groups assist H-spillover.

Alternatively, it has been proposed that spill-over hydrogen could be reversibly stored on the carbon support as adsorbed H^+ on the surface and as electrons in bulk,[91] as proposed for H-spillover on reducible oxides, where H· gives its electron to a reducible metal cation of the oxide support and diffuses in the form of H^+.

Considering the surface chemistry of oxygen-containing carbon materials,[92] and the reducing condition during H-spillover, equivalent to activated hydrogen,[64] the formation of the new primary and secondary alcohols is rationalized *via* the mechanisms shown in Scheme 2.

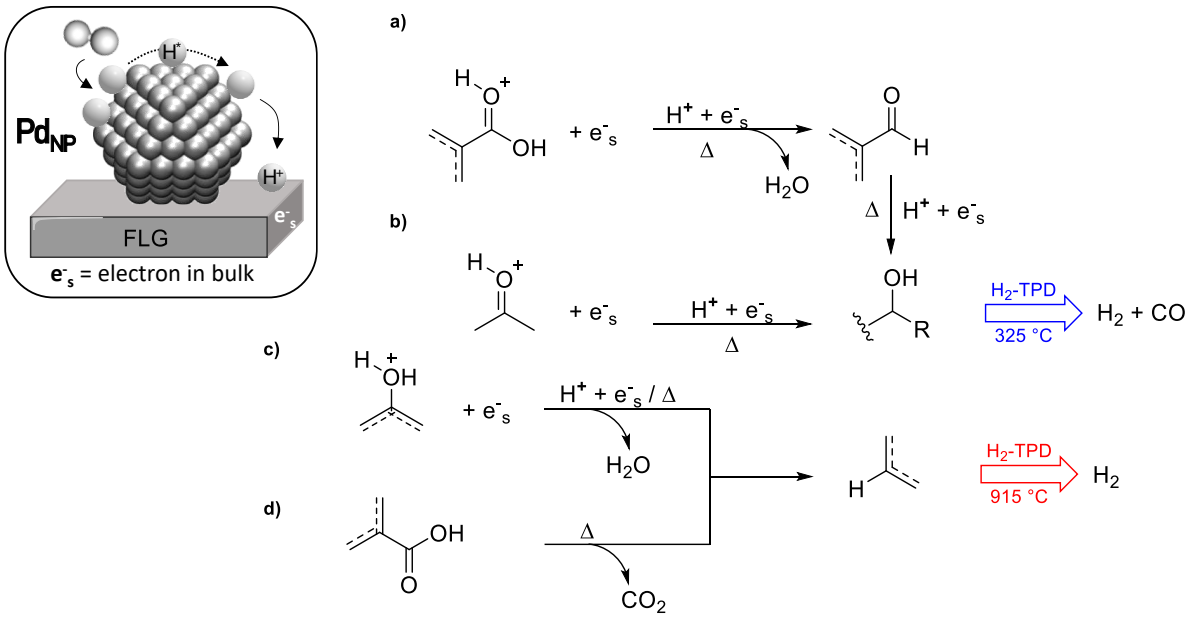

Scheme 2. Proposed pathway for reduction of surface oxygen groups assisted by H-spillover during the exothermic squalene hydrogenation reaction on the Pd/FLG catalyst.

Whether the reducing species is a physisorbed H· or a proton on a reduced surface, the alcohol functional groups should be readily obtainable from carboxylic acids and ketones, two species suspected to be involved in H-spillover. Starting from a carboxylic acid, the corresponding aldehyde can be obtained by sequentially adding two formal H· followed by water loss at high temperature. The aldehyde is rapidly reduced into the expected alcohol (Scheme **2a**, R = H) *vide supra* for computational details. Alcohols can also be directly obtained by the reduction of

ketones *via* the addition of two H· (Scheme **2b**, R = C, *vide supra* for computational details). Besides, the Pd/FLG catalysts display additional stable C – H bonds. The formation of these species is envisioned to proceed through the reduction of phenols by adding two H· under H-spillover and thermal reaction conditions (Scheme **2c**). A purely thermal pathway is also proposed from carboxylic acids *via* a thermal decarboxylation step (Scheme **2d**).

To confirm the origin of catalyst deactivation, the H-spillover was experimentally probed for the fresh and used Pd/FLG catalyst. As shown in the photographs of Figure S21, after 10 min at 40 °C, the WO_3 alone exhibited an unchanged color. When mixed with 2.5 mg of the fresh Pd/FLG catalyst, the dark blue color characteristic of H_xWO_3 is observed. When mixed with 2.5 mg of the used Pd/FLG catalyst, only a slight color change is observed, indicating a very limited H-spillover on the deactivated catalyst. Finally, we have also treated the fresh Pd/FLG catalyst at 600 °C under argon in order to eliminate the carboxylic groups. The heat-treated sample shows a slightly higher mean Pd_{NP} size (3.5 nm). When mixed with 2.5 mg of this catalyst, only a slight color change is observed during the WO_3 test (Figure S22), indicating a very limited H-spillover on this defunctionalized catalyst.

Conclusion

Palladium catalysts containing both Pd_{SA} and Pd_{NP} supported on CNT and FLG were prepared, characterized, and their catalytic activities in the hydrogenation of solvent-free squalene were evaluated. Both catalysts present similar Pd_{NP} sizes and few differences in charge transfer. An optimal Pd_{SA}/Pd_{NP} ratio and an extended H-spillover were measured for the Pd/FLG catalyst. The catalytic activity of Pd/CNT and Pd/FLG showed a tremendous improvement compared to previously described and/or commercially available catalysts. The solvent-free total reduction of squalene into squalane was effective at 120 °C, 30 bar H_2, using 60 ppm of Pd in less than 5

h. The catalysts' effectiveness could be attributed to a synergistic effect between a high Pd_{SA}/Pd_{NP} ratio and an H-spillover involving surface oxygenated functional groups on the prepared supports. Pd/FLG, presenting higher H-spillover performance, shows much higher initial catalytic activity and exothermicity compared to Pd/CNT but deactivated rapidly under those conditions.

Comparing the catalysts before and after the reaction reveals that coking, metal leaching, or sintering are not the reason for catalyst deactivation. Although the extended H-spillover on Pd/FLG catalyst is at the origin of its extremely high activity, it is also responsible (in combination with the generated heat) for its deactivation due to the reduction of surface oxygen-containing functional groups that are necessary for the H-spillover to operate.

Acknowledgements

This work was supported by the Agence Nationale de la Recherche (ANR-19-CE07-0030, COMET), which is gratefully acknowledged. We thank Vincent Collière (LCC, UPR8241 CNRS, Toulouse, France) for STEM analysis. J.N.-R., I.D.R., and I.C.G. acknowledge the "Calcul en Midi-Pyrénées" initiative CALMIP (projects p0812 and p1214) for the computer resources. The authors also thankfully acknowledge the HPC resources at CINES, IDRIS, and TGCC under the allocation 2022-A0120906649 made by GENCI.

Funding Sources

Agence Nationale de la Recherche (ANR-19-CE07-0030, COMET)

References

[1] M.A. Stoffels, F.J.R. Klauck, T. Hamadi, F. Glorius, J. Leker, Technology Trends of Catalysts in Hydrogenation Reactions: A Patent Landscape Analysis, Adv. Synth. Catal., 362 (2020) 1258-1274.

[2] F. Zaera, Designing Sites in Heterogeneous Catalysis: Are We Reaching Selectivities Competitive With Those of Homogeneous Catalysts?, Chem. Rev., 122 (2022) 8594-8757.

[3] L. Liu, A. Corma, Metal Catalysts for Heterogeneous Catalysis: From Single Atoms to Nanoclusters and Nanoparticles, Chem. Rev., 118 (2018) 4981-5079.

[4] H. Tian, X. Li, L. Zeng, J. Gong, Recent Advances on the Design of Group VIII Base-Metal Catalysts with Encapsulated Structures, ACS Catal., 5 (2015) 4959-4977.

[5] J. Liu, Catalysis by Supported Single Metal Atoms, ACS Catal., 7 (2017) 34-59.

[6] D. Pham Minh, P. Serp, Introduction to Supported Metal Single Atom Catalysis, in: P. Serp, D. Pham Minh (Eds.) Supported Metal Single Atom Catalysis, WILEY-VCH GmbH, 2022, pp. 1-49.

[7] P. Serp, Cooperativity in supported metal single atom catalysis, Nanoscale, 13 (2021) 5985-6004.

[8] S. Mitchell, J. Pérez-Ramírez, Single atom catalysis: a decade of stunning progress and the promise for a bright future, Nat. Commun., 11 (2020) 4302.

[9] F.D. Speck, J.H. Kim, G. Bae, S.H. Joo, K.J.J. Mayrhofer, C.H. Choi, S. Cherevko, Single-Atom Catalysts: A Perspective toward Application in Electrochemical Energy Conversion, JACS Au, 1 (2021) 1086-1100.

[10] X. Liang, N. Fu, S. Yao, Z. Li, Y. Li, The Progress and Outlook of Metal Single-Atom-Site Catalysis, J. Am. Chem. Soc., 144 (2022) 18155-18174.

[11] R.C. Contreras, B. Guicheret, B.F. Machado, C. Rivera-Cárcamo, M.A. Curiel Alvarez, B. Valdez Salas, M. Ruttert, T. Placke, A. Favre Réguillon, L. Vanoye, C. de Bellefon, R. Philippe, P. Serp, Effect of mesoporous carbon support nature and pretreatments on palladium loading, dispersion and apparent catalytic activity in hydrogenation of myrcene, J. Catal., 372 (2019) 226-244.

[12] C. Rivera-Cárcamo, I.C. Gerber, I. del Rosal, B. Guicheret, R. Castro Contreras, L. Vanoye, A. Favre-Réguillon, B.F. Machado, J. Audevard, C. de Bellefon, R. Philippe, P. Serp, Control of the single atom/nanoparticle ratio in Pd/C catalysts to optimize the cooperative hydrogenation of alkenes, Catal. Sci. Technol., 11 (2021) 984-999.

[13] L. Vanoye, B. Guicheret, C. Rivera-Cárcamo, R. Castro Contreras, C. de Bellefon, V. Meille, P. Serp, R. Philippe, A. Favre-Réguillon, Process intensification of the catalytic hydrogenation of squalene using a Pd/CNT catalyst combining nanoparticles and single atoms in a continuous flow reactor, Chem. Eng. J., 441 (2022) 135951.

[14] J. Audevard, A. Benyounes, R. Castro Contreras, H. Abou Oualid, M. Kacimi, P. Serp, Multifunctional Catalytic Properties of Pd/CNT Catalysts for 4-Nitrophenol Reduction, ChemCatChem, 14 (2022) e202101783.

[15] V.K. Soni, R.K. Sharma, Palladium-Nanoparticles-Intercalated Montmorillonite Clay: A Green Catalyst for the Solvent-Free Chemoselective Hydrogenation of Squalene, ChemCatChem, 8 (2016) 1763-1768.

[16] V. Pandarus, R. Ciriminna, F. Béland, M. Pagliaro, S. Kaliaguine, Solvent-Free Chemoselective Hydrogenation of Squalene to Squalane, ACS Omega, 2 (2017) 3989-3996.

[17] B. Guicheret, L. Vanoye, C. Rivera-Cárcamo, C. de Bellefon, P. Serp, R. Philippe, A. Favre-Réguillon, Solvent-Free Hydrogenation of Squalene Using Parts per Million Levels of Palladium Supported on Carbon Nanotubes: Shift from Batch Reactor to Continuous-Flow System, ChemSusChem, 15 (2022) e202200916.

[18] C.-T. Kuo, Y. Lu, L. Kovarik, M. Engelhard, A.M. Karim, Structure Sensitivity of Acetylene Semi-Hydrogenation on Pt Single Atoms and Subnanometer Clusters, ACS Catalysis, 9 (2019) 11030-11041.

[19] A. Borodziński,M. Bonarowska, Relation between Crystallite Size and Dispersion on Supported Metal Catalysts, Langmuir 13 (1997) 5613-5620.

[20] T. Placke, V. Siozios, S. Rothermel, P. Meister, C. Colle, M. Winter, Assessment of Surface Heterogeneity: a Route to Correlate and Quantify the 1st Cycle Irreversible Capacity Caused by SEI Formation to the Various Surfaces of Graphite Anodes for Lithium Ion Cells, Z. Phys. Chem., 229 (2015) 1451-1469.

[21] J.P. Olivier, M. Winter, Determination of the absolute and relative extents of basal plane surface area and “non-basal plane surface” area of graphites and their impact on anode performance in lithium ion batteries, J. Power Sources, 97-98 (2001) 151-155.

[22] S. Khoobiar, Particle to Particle Migration of Hydrogen Atoms on Platinum—Alumina Catalysts from Particle to Neighboring Particles, J. Phys. Chem., 68 (1964) 411-412.

[23] G. Kresse, J. Furthmüller, Efficiency of ab-initio total energy calculations for metals and semiconductors using a plane-wave basis set, Comput. Mater. Sci., 6 (1996) 15-50.

[24] G. Kresse, J. Furthmüller, Efficient iterative schemes for ab initio total-energy calculations using a plane-wave basis set, Phys. Rev. B 54 (1996) 11169-11186.

[25] J.P. Perdew, K. Burke, M. Ernzerhof, Generalized Gradient Approximation Made Simple, Phys. Rev. Lett., 77 (1996) 3865-3868.

[26] S. Grimme, J. Antony, S. Ehrlich, H. Krieg, A consistent and accurate ab initio parametrization of density functional dispersion correction (DFT-D) for the 94 elements H-Pu, J. Chem. Phys., 132 (2010) 154104.

[27] P.E. Blöchl, Projector augmented-wave method, Phys. Rev. B 50 (1994) 17953-17979.

[28] G. Kresse, D. Joubert, From ultrasoft pseudopotentials to the projector augmented-wave method, Phys. Rev. B 59 (1999) 1758-1775.

[29] J. Navarro-Ruiz, C. Rivera-Cárcamo, B. Machado, P. Serp, I. Del Rosal, I.C. Gerber, Computational Design of Pd Nanoclusters and Pd Single-Atom Catalysts Supported on O-Functionalized Graphene, ACS Appl. Nano Mater., 4 (2021) 12235-12249.

[30] H.J. Monkhorst, J.D. Pack, Special points for Brillouin-zone integrations, Phys. Rev. B 13 (1976) 5188-5192.

[31] G. Makov, M.C. Payne, Periodic boundary conditions in ab initio calculations, Phys. Rev. B 51 (1995) 4014-4022.

[32] G. Henkelman, H. Jónsson, Improved tangent estimate in the nudged elastic band method for finding minimum energy paths and saddle points, J. Chem. Phys., 113 (2000) 9978-9985.

[33] G. Henkelman, B.P. Uberuaga, H. Jónsson, A climbing image nudged elastic band method for finding saddle points and minimum energy paths, J. Chem. Phys., 113 (2000) 9901-9904.

[34] C. Rivera-Cárcamo, C. Scarfiello, A.B. García, Y. Tison, H. Martinez, W. Baaziz, O. Ersen, C. Le Berre, P. Serp, Stabilization of Metal Single Atoms on Carbon and TiO_2 Supports for CO_2 Hydrogenation: The Importance of Regulating Charge Transfer, Adv. Mater. Interfaces, 8 (2021) 2001777.

[35] I.C. Gerber, P. Serp, A Theory/Experience Description of Support Effects in Carbon-Supported Catalysts, Chem. Rev., 120 (2020) 1250-1349.

[36] S. Dong Jin, P. Tae-Jin, I. Son-Ki, Effect of surface oxygen groups of carbon supports on the characteristics of Pd/C catalysts, Carbon, 31 (1993) 427-435.

[37] X. Lu, C. Guo, M. Zhang, L. Leng, J.H. Horton, W. Wu, Z. Li, Rational design of palladium single-atoms and clusters supported on silicoaluminophosphate-31 by a

photochemical route for chemoselective hydrodeoxygenation of vanillin, Nano Res., 14 (2021) 4347-4355.

[38] Q. Shen, H. Jin, P. Li, X. Yu, L. Zheng, W. Song, C. Cao, Breaking the activity limitation of iridium single-atom catalyst in hydrogenation of quinoline with synergistic nanoparticles catalysis, Nano Res., 15 (2022) 5024-5031.

[39] L. Kuai, Z. Chen, S. Liu, E. Kan, N. Yu, Y. Ren, C. Fang, X. Li, Y. Li, B. Geng, Titania supported synergistic palladium single atoms and nanoparticles for room temperature ketone and aldehydes hydrogenation, Nat. Commun., 11 (2020) 48.

[40] L. Ning, S. Liao, H. Li, R. Tong, C. Dong, M. Zhang, W. Gu, X. Liu, Carbon-based materials with tunable morphology confined Ni (0) and Ni-Nx active sites: Highly efficient selective hydrogenation catalysts, Carbon, 154 (2019) 48-57.

[41] R.R. Bacsa, I. Cameán, A. Ramos, A.B. Garcia, V. Tishkova, W.S. Bacsa, J.R. Gallagher, J.T. Miller, H. Navas, V. Jourdain, M. Girleanu, O. Ersen, P. Serp, Few layer graphene synthesis on transition metal ferrite catalysts, Carbon, 89 (2015) 350-360.

[42] L.G. Cançado, A. Jorio, E.H.M. Ferreira, F. Stavale, C.A. Achete, R.B. Capaz, M.V.O. Moutinho, A. Lombardo, T.S. Kulmala, A.C. Ferrari, Quantifying Defects in Graphene via Raman Spectroscopy at Different Excitation Energies, Nano Lett., 11 (2011) 3190-3196.

[43] K.G. Sun, J.S. Chung, S.H. Hur, Durability Improvement of Pt/RGO Catalysts for PEMFC by Low-Temperature Self-Catalyzed Reduction, Nanoscale Res. Lett., 10 (2015) 257.

[44] M. Smith, L. Scudiero, J. Espinal, J.-S. McEwen, M. Garcia-Perez, Improving the deconvolution and interpretation of XPS spectra from chars by ab initio calculations, Carbon, 110 (2016) 155-171.

[45] H. Darmstadt, C. Roy, Surface spectroscopic study of basic sites on carbon blacks, Carbon, 41 (2003) 2662-2665.

[46] P. Brender, R. Gadiou, J.-C. Rietsch, P. Fioux, J. Dentzer, A. Ponche, C. Vix-Guterl, Characterization of Carbon Surface Chemistry by Combined Temperature Programmed Desorption with in Situ X-ray Photoelectron Spectrometry and Temperature Programmed Desorption with Mass Spectrometry Analysis, Anal. Chem., 84 (2012) 2147-2153.

[47] N. Li, X. Ma, Q. Zha, K. Kim, Y. Chen, C. Song, Maximizing the number of oxygen-containing functional groups on activated carbon by using ammonium persulfate and improving the temperature-programmed desorption characterization of carbon surface chemistry, Carbon, 49 (2011) 5002-5013.

[48] M.L. Godino-Salido, R. López-Garzón, M.D. Gutiérrez-Valero, P. Arranz-Mascarós, M. Melguizo-Guijarro, M.D. López de la Torre, V. Gómez-Serrano, M. Alexandre-Franco, D. Lozano-Castelló, D. Cazorla-Amorós, M. Domingo-García, Effect of the surface chemical groups of activated carbons on their surface adsorptivity to aromatic adsorbates based on π-π interactions, Mater. Chem. Phys., 143 (2014) 1489-1499.

[49] J.-H. Zhou, Z.-J. Sui, J. Zhu, P. Li, D. Chen, Y.-C. Dai, W.-K. Yuan, Characterization of surface oxygen complexes on carbon nanofibers by TPD, XPS and FT-IR, Carbon, 45 (2007) 785-796.

[50] M. Göckeler, C.M. Berger, M. Purcel, R. Bergsträßer, A.-P. Schinkel, M. Muhler, Surface reactions during temperature-programmed desorption and reduction experiments with oxygen-functionalized carbon blacks, Appl. Surf. Sci., 561 (2021) 150044.

[51] J.F. Vivo-Vilches, E. Bailón-García, A.F. Pérez-Cadenas, F. Carrasco-Marín, F.J. Maldonado-Hódar, Tailoring the surface chemistry and porosity of activated carbons: Evidence of reorganization and mobility of oxygenated surface groups, Carbon, 68 (2014) 520-530.

[52] B. Marchon, J. Carrazza, H. Heinemann, G.A. Somorjai, TPD and XPS studies of O_2, CO_2, and H_2O adsorption on clean polycrystalline graphite, Carbon, 26 (1988) 507-514.

[53] S.A. Chernyak, A.S. Ivanov, A.M. Podgornova, E.A. Arkhipova, S.Y. Kupreenko, A.V. Shumyantsev, N.E. Strokova, K.I. Maslakov, S.V. Savilov, V.V. Lunin, Kinetics of the defunctionalization of oxidized few-layer graphene nanoflakes, Phys. Chem. Chem. Phys., 20 (2018) 24117-24122.

[54] V.M. Shinde, E. Skupien, M. Makkee, Synthesis of highly dispersed Pd nanoparticles supported on multi-walled carbon nanotubes and their excellent catalytic performance for oxidation of benzyl alcohol, Catal. Sci. Technol., 5 (2015) 4144-4153.

[55] I. Janowska, M.-S. Moldovan, O. Ersen, H. Bulou, K. Chizari, M.J. Ledoux, C. Pham-Huu, High temperature stability of platinum nanoparticles on few-layer graphene investigated by In Situ high resolution transmission electron microscopy, Nano Res., 4 (2011) 511-521.

[56] A. Borodziński, M. Bonarowska, Relation between Crystallite Size and Dispersion on Supported Metal Catalysts, Langmuir, 13 (1997) 5613-5620.

[57] B.-H. Mao, C.-H. Liu, X. Gao, R. Chang, Z. Liu, S.-D. Wang, In situ characterization of catalytic activity of graphene stabilized small-sized Pd nanoparticles for CO oxidation, Appl. Surf. Sci., 283 (2013) 1076-1079.

[58] R.G. Rao, R. Blume, M.T. Greiner, P. Liu, T.W. Hansen, K.S. Dreyer, D.D. Hibbitts, J.-P. Tessonnier, Oxygen-Doped Carbon Supports Modulate the Hydrogenation Activity of Palladium Nanoparticles through Electronic Metal–Support Interactions, ACS Catal., 12 (2022) 7344-7356.

[59] V. V. Chesnokov, I. P. Prosvirin, N. A. Zaitseva, V. I. Zaikovskii, V. V. Molchanov, Effect of the Structure of Carbon Nanofibers on the State of an Active Component and on the Catalytic Properties of Pd/C Catalysts in the Selective Hydrogenation of 1,3-Butadiene, Kinet. Catal., 43 (2002) 838-846.

[60] J. Navarro-Ruiz, R. Poteau, I.C. Gerber, I. del Rosal, Contribution of Theoretical Calculations to Supported Metal Single-Atom Catalysis, in: P. Serp, D. Pham Minh (Eds.) Supported Metal Single Atom Catalysis, 2022, pp. 241-337.

[61] B.F. Machado, M. Oubenali, M. Rosa Axet, T. Trang Nguyen, M. Tunckol, M. Girleanu, O. Ersen, I.C. Gerber, P. Serp, Understanding the surface chemistry of carbon nanotubes: Toward a rational design of Ru nanocatalysts, J. Catal., 309 (2014) 185-198.

[62] K. Takeuchi, S. Yamamoto, Y. Hamamoto, Y. Shiozawa, K. Tashima, H. Fukidome, T. Koitaya, K. Mukai, S. Yoshimoto, M. Suemitsu, Y. Morikawa, J. Yoshinobu, I. Matsuda, Adsorption of CO_2 on Graphene: A Combined TPD, XPS, and vdW-DF Study, J. Phys. Chem. C, 121 (2017) 2807-2814.

[63] Z. Lendzion-Bieluń, Ł. Czekajło, D. Sibera, D. Moszyński, J. Sreńscek-Nazzal, A.W. Morawski, R.J. Wrobel, B. Michalkiewicz, W. Arabczyk, U. Narkiewicz, Surface characteristics of KOH-treated commercial carbons applied for CO_2 adsorption, Adsorpt. Sci. Technol., 36 (2017) 478-492.

[64] Z. Zheng, M. Chen, X. Zheng, K. Liu, T. Yang, J. Zhang, Hydrogen Spillover Facilitating Reduction of Surface Oxygen Species on Porous Carbon, ChemistrySelect, 6 (2021) 2178-2183.

[65] Y.-X. Tuo, L.-J. Shi, H.-Y. Cheng, Y.-A. Zhu, M.-L. Yang, J. Xu, Y.-F. Han, P. Li, W.-K. Yuan, Insight into the support effect on the particle size effect of Pt/C catalysts in dehydrogenation, J. Catal., 360 (2018) 175-186.

[66] Z. Huang, Y. Yao, Z. Pang, Y. Yuan, T. Li, K. He, X. Hu, J. Cheng, W. Yao, Y. Liu, A. Nie, S. Sharifi-Asl, M. Cheng, B. Song, K. Amine, J. Lu, T. Li, L. Hu, R. Shahbazian-Yassar, Direct observation of the formation and stabilization of metallic nanoparticles on carbon supports, Nat Commun., 11 (2020) 6373.

[67] B. Gerand, M. Figlarz, Reduction of Hexagonal WO3 by Hydrogen Spillover : Formation of New Hydrogen Hexagonal Tungsten Bronzes $HxWO_3$, in: G.M. Pajonk, S.J. Teichner, J.E. Germain (Eds.) Stud. Surf. Sci. Catal., Elsevier, 1983, pp. 275-283.

[68] F. Benseradj, F. Sadi, M. Chater, Hydrogen spillover studies on diluted Rh/Al_2O_3 catalyst, Appl. Catal., A, 228 (2002) 135-144.

[69] A.D. Lueking, R.T. Yang, Hydrogen spillover to enhance hydrogen storage—study of the effect of carbon physicochemical properties, Appl. Catal., A, 265 (2004) 259-268.

[70] K. Fisher, S. Schofer, Jessica, D. Kanne, B., Squalane and isosqualane compositions and methods for preparing the same, Amyris Biotechnologies, Inc., USA, WO patent 2011146837, (2011).

[71] K. Fisher, F. Woolard, X, Farnesene dimers and/or farnesane dimers and composition thereof in, Amyris Biotechnologies, Inc., USA, WO patent 2010042208, (2010).

[72] W. Guohua, S. Haihui, X. Zhihua, G. Meiqing, Z. Wenliang, L. Yingjun, Plant Squalene Composition and preparation method therefor and application thereof, and product applying same in, Yichun Dahaigui Life Science Co ltd, WO Patent 2019/214410, (2019).

[73] K. Sogabe, T. Koshiyama, High-purity and low-malodorous squalane and method for producing the same, in, New Japan Chemical Co Ltd, JP patent 2008013477A (https://patents.google.com/patent/JP3173649B2/en), (2008).

[74] J.M. Vila Peris, M. Alamany Soler, R. Celades Colom, A process for the preparation of hexamethyl tetracosanes, in, Hispano Quimica SA, EP patent 0228980A1, (1986).

[75] G. Xie, G. Wei, Z. Xiong, W. Zhang, H. Sun, Z. Ouyang, L. Peng, Y. Liao, Plant squalene composition and preparation method therefore and application thereof, and product applying same in, Yichun Dahaigui Life Science Co ltd, WO patent 2019214410A1, (2019).

[76] P. Albers, J. Pietsch, S.F. Parker, Poisoning and deactivation of palladium catalysts, J. Mol. Catal. A: Chem., 173 (2001) 275-286.

[77] P.-H. Jen, Y.-H. Hsu, S.D. Lin, The activity and stability of Pd/C catalysts in benzene hydrogenation, Catal. Today, 123 (2007) 133-141.

[78] J.A. Menéndez, L.R. Radovic, B. Xia, J. Phillips, Low-Temperature Generation of Basic Carbon Surfaces by Hydrogen Spillover, J. Phys. Chem., 100 (1996) 17243-17248.

[79] V.H. Pham, T.T. Dang, K. Singh, S.H. Hur, E.W. Shin, J.S. Kim, M.A. Lee, S.H. Baeck, J.S. Chung, A catalytic and efficient route for reduction of graphene oxide by hydrogen spillover, J. Mater. Chem. A, 1 (2013) 1070-1077.

[80] B.K. Barman, K.K. Nanda, Rapid reduction of GO by hydrogen spill-over mechanism by in situ generated nanoparticles at room temperature and their catalytic performance towards 4-nitrophenol reduction and ethanol oxidation, Appl. Catal., A, 491 (2015) 45-51.

[81] S. Reiche, R. Blume, X.C. Zhao, D. Su, E. Kunkes, M. Behrens, R. Schlögl, Reactivity of mesoporous carbon against water – An in-situ XPS study, Carbon, 77 (2014) 175-183.

[82] R. Burgess, C. Buono, P.R. Davies, R.J. Davies, T. Legge, A. Lai, R. Lewis, D.J. Morgan, N. Robinson, D.J. Willock, The functionalisation of graphite surfaces with nitric acid: Identification of functional groups and their effects on gold deposition, J. Catal., 323 (2015) 10-18.

[83] D. Rosenthal, M. Ruta, R. Schlögl, L. Kiwi-Minsker, Combined XPS and TPD study of oxygen-functionalized carbon nanofibers grown on sintered metal fibers, Carbon, 48 (2010) 1835-1843.

[84] Y.-C. Chiang, W.-H. Lin, Y.-C. Chang, The influence of treatment duration on multi-walled carbon nanotubes functionalized by H_2SO_4/HNO_3 oxidation, Appl. Surf. Sci., 257 (2011) 2401-2410.

[85] E.W. Shin, S.-I. Cho, J.H. Kang, W.J. Kim, J.D. Park, S.H. Moon, Palladium-hydrogen interaction on supported palladium catalysts of different metal dispersions, Korean J. Chem. Eng., 17 (2000) 468-472.

[86] P.J. Berlowitz, D.W. Goodman, Chemisorption of ultrathin palladium layers on tungsten(110) and tungsten(100): adsorption of hydrogen and carbon monoxide, Langmuir, 4 (1988) 1091-1095.

[87] F. Coloma, A. Sepúlveda-Escribano, J.L.G. Fierro, F. Rodríguez-Reinoso, Gas phase hydrogenation of crotonaldehyde over Pt/Activated carbon catalysts. Influence of the oxygen surface groups on the support, Appl. Catal., A, 150 (1997) 165-183.

[88] A.B. Trenwith, Thermal decomposition of isopropanol, J. Chem. Soc., Faraday Trans. 1, 71 (1975) 2405-2412.

[89] U. Roland, T. Braunschweig, F. Roessner, On the nature of spilt-over hydrogen, J. Mol. Catal. A: Chem., 127 (1997) 61-84.

[90] M. Tan, Y. Yang, Y. Yang, J. Chen, Z. Zhang, G. Fu, J. Lin, S. Wan, S. Wang, Y. Wang, Hydrogen spillover assisted by oxygenate molecules over nonreducible oxides, Nat. Commun., 13 (2022) 1457.

[91] F. Yang, B. Hu, W. Xia, B. Peng, J. Shen, M. Muhler, On the nature of spillover hydrogen species on platinum/nitrogen-doped mesoporous carbon composites: A temperature-programmed nitrobenzene desorption study, J. Catal., 365 (2018) 55-62.

[92] J.L. Figueiredo, M.F.R. Pereira, The role of surface chemistry in catalysis with carbons, Catal. Today, 150 (2010) 2-7.